

Benchmarking Kinetic Calculations of Resistive Wall Mode Stability

J.W. Berkery,¹ Y.Q. Liu,² Z.R. Wang,³ S.A. Sabbagh,¹ N.C. Logan,³ J.-K. Park,³ J. Manickam,³ and R. Betti⁴

¹*Department of Applied Physics and Applied Mathematics, Columbia University, New York, New York 10027*

²*Euratom/CCFE Fusion Association, Culham Science Centre, Abingdon, OX14 3DB, UK*

³*Princeton Plasma Physics Laboratory, Princeton University, Princeton, New Jersey 08543*

⁴*Laboratory for Laser Energetics, University of Rochester, Rochester, New York 14623*

(Dated: 7 March 2014)

Validating the calculations of kinetic resistive wall mode (RWM) stability is important for confidently predicting RWM stable operating regions in ITER and other high performance tokamaks for disruption avoidance. Benchmarking the calculations of the MARS-K [Y. Liu, *et al.*, Phys. Plasmas **15**, 112503 (2008)], MISK [B. Hu, *et al.*, Phys. Plasmas **12**, 057301 (2005)], and PENT [N. Logan, *et al.*, accepted by Phys. Plasmas (2013)] codes for two Solov'ev analytical equilibria and a projected ITER equilibrium has demonstrated good agreement between the codes. The important particle frequencies, the frequency resonance energy integral in which they are used, the marginally stable eigenfunctions, perturbed Lagrangians, and fluid growth rates are all generally consistent between the codes. The most important kinetic effect at low rotation is the resonance between the mode rotation and the trapped thermal particle's precession drift, and MARS-K, MISK, and PENT show good agreement in this term. The different ways the rational surface contribution was treated historically in the codes is identified as a source of disagreement in the bounce and transit resonance terms at higher plasma rotation. Calculations from all of the codes support the present understanding that RWM stability can be increased by kinetic effects at low rotation through precession drift resonance and at high rotation by bounce and transit resonances, while intermediate rotation can remain susceptible to instability. The applicability of benchmarked kinetic stability calculations to experimental results is demonstrated by the prediction of MISK calculations of near marginal growth rates for experimental marginal stability points from the National Spherical Torus Experiment (NSTX) [M. Ono, *et al.*, Nucl. Fusion **40**, 557 (2000)]. © 2014 American Institute of Physics. [DOI: 00.0000/0.0000000]

I. INTRODUCTION

Tokamak fusion plasmas generate energy most efficiently when the ratio of plasma stored energy to magnetic confining field energy is high. In this regime, the plasma is subject to magnetohydrodynamic (MHD) kink-ballooning instabilities. This can lead to a disruption of the plasma current and a loss of confinement on the relatively short Alfvén time scale. However, the growth rate of this mode can be slowed quite considerably by the presence of a close-fitting wall around the plasma. The magnetic perturbation from the mode can penetrate the wall during mode growth, and the time scale for that penetration is much longer than the Alfvén time scale. When the mode is converted to the more slowly growing mode in this way, it is called the resistive wall mode (RWM)¹.

Originally it was thought that the presence of a resistive wall could slow down the kink-ballooning mode, but that the RWM itself could not be stabilized. Experiments soon found, however, that tokamaks could be stably operated above the so-called “no-wall limit”^{2,3}. It was then postulated theoretically that the RWM can be stabilized by a combination of plasma rotational inertia and an energy dissipation mechanism⁴⁻⁶. Simple models proved to be insufficient to explain experimental results^{3,7-9}, and theoretical investigation has turned to the inclusion of kinetic effects to explain the plasma stability¹⁰⁻³².

One can calculate the stability of the RWM by de-

termining $\omega = \omega_r + i\gamma$, the complex mode frequency, where ω_r is the real mode rotation frequency, and γ is the growth rate. A standard approach is to change the force balance equation into an equation in terms of changes of kinetic and potential energies (δW), and then to write a dispersion relation for the complex mode frequency ω in terms of these δW terms³³⁻³⁵. Specifically applicable to the RWM is the so-called “low-frequency” energy principle³⁴⁻³⁸, which requires the inclusion of the particle drift frequencies, as these can not be considered to be much lower than the mode frequency. The approach of solving for the δW terms has the advantage of clarity in distinguishing the various stabilizing and destabilizing effects. In this work we will concentrate on the change of potential energy that arises from the perturbed kinetic pressure of thermal particles.

The RWM dispersion relation can be written^{10,11,14}:

$$(\gamma + i\omega_r)\tau_w = - \frac{\delta W_\infty + \delta W_K}{\delta W_b + \delta W_K}. \quad (1)$$

Here τ_w is the current decay time in the resistive wall, δW_∞ is the sum of the plasma fluid and vacuum perturbed potential energies when the wall is placed at infinity, and δW_b is the sum of the plasma fluid and vacuum δW s when the wall is placed at a specific location b . These two contributions to the energy principle have been theoretically developed for years³⁹, and computer codes have been written to solve for them, such as PEST⁴⁰. The

kinetic term, δW_K is given by

$$\delta W_K = -\frac{1}{2} \sum_j \int \xi_{\perp}^* \cdot [\nabla \cdot \tilde{\mathbb{P}}_K] dV, \quad (2)$$

where ξ_{\perp} is the mode displacement. In the fluid approach the perturbed pressure is given in terms of macroscopic quantities. In the kinetic approach the components of the pressure tensor $\tilde{\mathbb{P}}_K$, \tilde{p}_{\perp} and \tilde{p}_{\parallel} , are defined by taking moments of the perturbed distribution function \tilde{f} . The kinetic approach allows for resonances between the mode rotation and particle precession, bounce, or transit frequencies that can transfer energy from the mode to the particles and thereby maintain the stability of the RWM.

The goal of this work is to benchmark calculations of kinetic resistive wall mode stability. This effort was initiated and conducted through an International Tokamak Physics Activity (ITPA) of the MHD Stability group. Three codes, MARS-K^{14,41}, MISK¹¹, and PENT⁴² are compared in detail in this work. The PENT code was largely written during this effort. This work builds off of, and greatly expands upon, a previous effort in which the MARS-K and MISHKA+HAGIS^{43,44} codes were benchmarked in Ref. [14], Sec. III-C.

The ITPA MHD Stability Group proponents decided upon a group of common equilibria to test, and a set of constraints were determined to allow direct comparisons between the codes. It was decided to compare code calculations for two analytical equilibria, one a simple, near-circular shape with no $n = 1$ rational surfaces, and one a shaped equilibria with two $n = 1$ rational surfaces, as well as an ITER case. In each case the focus was on the calculation of rotational resonances of thermal particles, so collisions were ignored and energetic particles were not included. Though obviously important, it is beyond the scope of this work to fully compare stability calculations to present experimental results, though MISK calculations of RWM stability have been compared to both National Spherical Torus Experiment⁴⁵ (NSTX)^{19–22,24,46–48} and DIII-D^{9,25} experimental results, while MARS-K calculations have been performed for RWM stability in DIII-D^{18,41} and the RFX-mod reversed field pinch^{27,49,50}, as well as for ideal wall mode stability in NSTX⁵¹. Finally, comparisons between the benchmarked MISK calculations and NSTX results are also presented here. Benchmarking and experimentally validated calculations of RWM stability are important to confidently project the stability of future devices such as ITER, which can not tolerate disruptions.

The paper is organized as follows. First, the MARS-K, MISK, and PENT codes are briefly described in Sec. II. In Sec. III the equilibrium configurations that are tested are described. In Sec. IV various important frequencies of the plasma are compared, which are then used in Sec. V in the energy integral of the frequency resonance fraction. The three different eigenfunctions used are described in Sec. VI, and are then used in Sec. VII in calculating

the perturbed Lagrangian. The results of the resistive wall mode stability analysis are presented, starting in Sec. VIII with the fluid δW terms, in Sec. IX with the kinetic δW term, and in Sec. X with the RWM growth rate and rotation frequency. Finally, the benchmarked calculations of the MISK code are briefly compared to NSTX experiments in Sec. XI.

II. CODES

Various codes have been developed that can incorporate kinetic effects in stability calculations. In addition to the three described here, one prominent example is the combination of the MISHKA⁴³ and HAGIS⁴⁴ codes.

A. MARS-K

MARS-K (Magnetohydrodynamic Resistive Spectrum - Kinetic code) is a toroidal MHD-kinetic hybrid stability code^{14,41} that solves the eigenvalue problem derived from the linearized single-fluid ideal/resistive MHD equations with toroidal flow, self-consistently including the drift kinetic effects in full toroidal geometry. This approach allows the kinetic effects associated with the thermal or energetic particles to consistently modify the mode eigenfunction, which could significantly influence the mode stability and structure in certain circumstances³¹. In this work, however, MARS-K will be used in a perturbative mode.

MARS-K simulates a plasma surrounded by a pure vacuum region, a resistive wall, and a set of magnetic coils. With these features, the code can be applied to the physical study and support of experiments on various subjects such as MHD instabilities (e.g. resistive wall mode and tearing mode), and plasma response to external fields (e.g. resonant field amplification and resonant magnetic perturbation).

B. MISK

The MISK, or Modification to Ideal Stability by Kinetic effects, code¹¹ calculates the change in potential energy of the plasma due to kinetic effects, δW_K . Along with the fluid δW terms calculated using a marginally stable eigenfunction with the PEST code⁴⁰, the dispersion relation or energy principle including kinetic effects is used to predict the growth rate of the resistive wall mode. This approach assumes that kinetic effects do not change the eigenfunction, and that the mode growth rate and frequency are small, so their nonlinear inclusion is unimportant. Cases which are above the ideal no-wall limit, and therefore would be unstable without kinetic effects, are examined. MISK has been used extensively (see Refs. [19–25, 47, and 48]), and close quantitative agreement has been found between theoretically expected

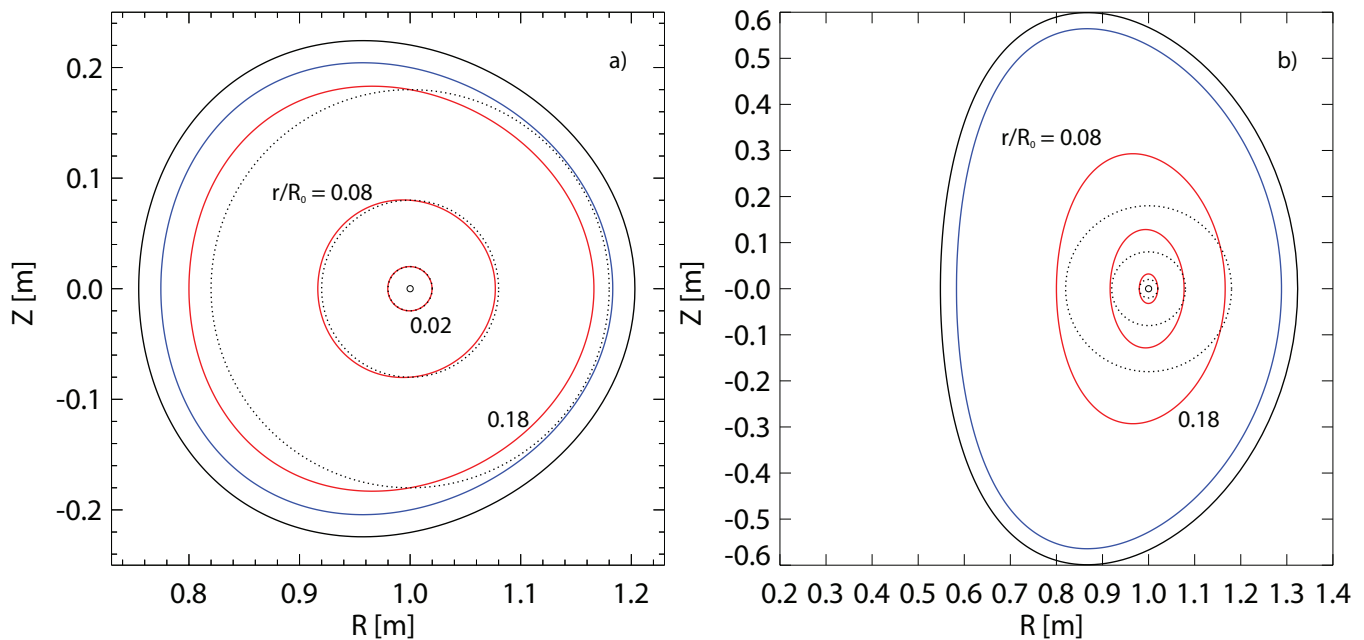


FIG. 1. a) The Solov'ev 1 equilibrium and b) the Solov'ev 3 equilibrium, showing flux surfaces at the edge (blue) and $r/R_0 = 0.02, 0.08,$ and 0.18 (red). These last three are compared to their equivalent circles (dashed). Finally, conformal walls having $r_w/a = 1.15$ for Solov'ev 1 and $r_w/a = 1.10$ for Solov'ev 3 are shown in black (see section VIII).

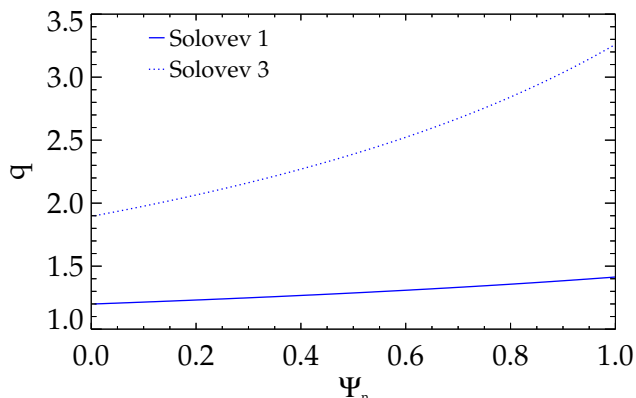


FIG. 2. The Solov'ev 1 and Solov'ev 3 equilibrium q profiles.

RWM marginal stability points and RWM stability in NSTX and DIII-D.

C. PENT

The PENT (Perturbed Equilibrium Nonambipolar Transport) code⁴² calculates the toroidal torque due to neoclassical toroidal viscosity (NTV)⁵² in a nonaxisymmetric equilibrium⁵³. In the perturbative approach with no mode rotation, the toroidal torque due to nonambipolar transport and the drift kinetic energy are related by a simple equivalency principle^{54,55}, $T_\phi = 2in\delta W_K$. The PENT code was developed in conjunction with the

IPEC⁵⁶ (Ideal Perturbed Equilibrium Code) and DCON⁵⁷ codes, which have been widely used and found to be in good agreement with experiment⁵⁸⁻⁶². Although originally developed to couple externally applied 3D fields to the plasma, this suite of codes is used with an equivalent approach to MISC and PEST for this benchmark. The fluid δW is calculated using the marginally stable eigenfunction from DCON which is used in IPEC to calculate the 3D perturbed equilibrium. The kinetic term calculated in PENT is then included in Eq. 1, which is valid only in the same small perturbation limit as the equivalency principle.

III. EQUILIBRIA

Three equilibria were used for this benchmarking exercise: an analytical equilibrium with nearly circular surfaces and no rational surfaces, an analytical equilibrium with shaped surfaces and two $n = 1$ rational surfaces, and finally a projected ITER equilibrium.

A. Solov'ev Equilibrium

The Solov'ev equilibrium^{63,64} is an analytical equilibrium solution to the Grad-Shafranov equation for the poloidal current function $F = RB_t$ (with R the major radius and B_t the toroidal magnetic field), and the pressure profile $P(\psi)$, where ψ is the magnetic flux coordinate. In MARS-K, the Solov'ev equilibrium is written¹⁴:

$$F(\psi) = 1. \quad (3)$$

$$\frac{\mu_0}{B_0^2} P(\psi) = -\frac{1 + \kappa^2}{\kappa R_0^3 q_0} \psi. \quad (4)$$

$$\psi = \frac{\kappa}{2R_0^3 q_0} \left[\frac{R^2 Z^2}{\kappa^2} + \frac{1}{4} (R^2 - R_0^2)^2 - \epsilon_a^2 R_0^4 \right]. \quad (5)$$

This ψ ranges from a negative value at the axis ($-\psi_0$) to zero at the edge. A normalized flux can be written $\Psi_n = \psi/\psi_0 + 1$, which goes from 0 on axis to 1 at the edge. In addition to B_0 , the magnetic field on axis, and R_0 , the major radius of the plasma axis, three quantities must be specified: the elongation κ , the safety factor on axis q_0 , and the inverse aspect ratio $\epsilon_a = a/R_0$, where a is the plasma minor radius. The plasma boundary is specified in (R, Z) coordinates by:

$$R_b = R_0 (1 + 2\epsilon_a \cos \theta)^{\frac{1}{2}}, \quad (6)$$

$$Z_b = \frac{R_0 \epsilon_a \kappa \sin \theta}{(1 + 2\epsilon_a \cos \theta)^{\frac{1}{2}}}. \quad (7)$$

Note also that for the Solov'ev cases, the q profile can be analytically determined from⁶⁵:

$$q = q_0 \frac{2\sqrt{1 + 2\epsilon_r}}{\pi(1 - 4\epsilon_r^2)} E(k), \quad (8)$$

where E is the complete elliptic integral of the second kind, $k \equiv \sqrt{4\epsilon_r/(1 + 2\epsilon_r)}$, and $\epsilon_r = (R - R_0)/R_0$.

MISK uses the PEST code and PENT uses the DCON code to provide the eigenfunction and fluid δW terms. The two differ in that the PEST calculation includes both potential and kinetic energy terms in δW , which allows typically resonant eigenfunction displacements to bridge the corresponding rational surfaces. DCON only includes a potential energy δW , and resonant components of eigenfunction displacement are forced to zero at the corresponding rational surfaces. The Solov'ev equilibrium can be explicitly specified in PEST and DCON.

1. Solov'ev 1

The equilibrium designated ‘‘Solov'ev 1’’ was used in Ref. [14], and is near-circular (Fig. 1a), with no $n = 1$ rational surfaces (Fig. 2). It is specified by the parameters $\kappa = 1$, $q_0 = 1.2$, and $\epsilon_a = 0.2$, and has a $q_{\text{edge}} = 1.41371$.

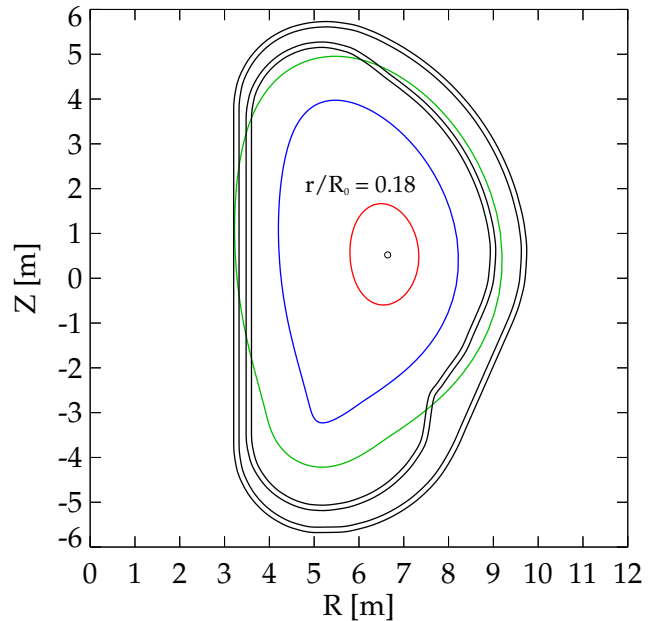


FIG. 3. The ITER equilibrium, showing a flux surface at the edge (blue) and $r/R_0 = 0.18$ (red). Also shown are the ITER double wall (black), and a conformal wall with $r_w/a = 1.5$ (green).

2. Solov'ev 3

The equilibrium designated ‘‘Solov'ev 3’’ was also used in Ref. [14]. This equilibrium is shaped (Fig. 1b), and contains the $q = 2$ and 3 rational surfaces within the plasma (Fig. 2). It is specified by the parameters $\kappa = 1.6$, $q_0 = 1.9$, and $\epsilon_a = 0.33$, and has a $q_{\text{edge}} = 3.263$.

B. ITER

The ITER equilibrium utilizes the current design of the ITER target for 9 MA operation⁶⁶, with $\beta_N = 2.9$. It has $R_0 = 6.2$ m, $B_0 = 5.3$ T, the shape shown in Fig. 3 and the q profile shown in Fig. 4.

IV. FREQUENCY COMPARISONS

A. Density, Temperature, Pressure, and Rotation Frequency Profiles

We will assume for the Solov'ev cases that there are no energetic particles, only thermal ions and electrons, and that the ion and electron densities and temperatures are equal, $n_e = n_i$ and $T_e = T_i$. Also, for the purposes of determining P from Eq. 4, we now set $R_0 = 1$ m and $B_0 = 1$ T. Then the pressure has the form $P = P_0(1 - \Psi_n)$, with

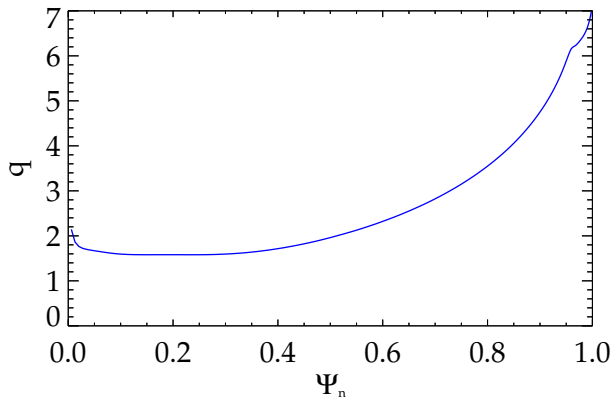


FIG. 4. The ITER equilibrium q profile.

$P_0 = 2.210 \times 10^4$ Pa for Solov'ev 1, and $P_0 = 4.273 \times 10^4$ Pa for Solov'ev 3.

Finally we must specify the density profile. For the Solov'ev cases, we use $n = n_0(1 - 0.7\Psi_n)$. Then the density on axis, n_0 , is determined by specifying $(\omega_{ci}/\omega_A)_0$, where the Alfvén frequency on axis $\omega_{A0} = B_0/(R_0\sqrt{\mu_0 m_i n_{i0}})$ and the ion cyclotron frequency on axis $\omega_{ci0} = eB_0/m_i = 47.9 \times 10^6$ krad/s. For the comparisons here, we will use $(\omega_{ci}/\omega_A)_0 = 121$, to be consistent with Ref. [14], even though this results in the values of $\omega_{A0} = 395.9$ krad/s and the unrealistically high density $n_0 = 1.518 \times 10^{21}$ m $^{-3}$. Note that the normalized mass density $\rho/\rho_0 = 1 - \Psi_n$ also affects the eigenfunction.

The temperature profile is then determined from $T = P/(2n)$. For the Solov'ev cases this means $T = (P_0/2n_0)(1 - \Psi_n)/(1 - 0.7\Psi_n)$.

For the Solov'ev cases we will use the $E \times B$ frequency profile $\omega_E = \omega_{E0}(1 - \Psi_n)$, and a range of constant values of ω_{E0} . We will take $\omega_{E0}/\omega_{A0} = 1 \times 10^{-2}$ or $\omega_{E0} = 3.959$ krad/s as a nominal value. The toroidal rotation frequency, ω_ϕ can then be found by a radial force balance neglecting poloidal rotation so that $\omega_\phi = \omega_E + \omega_{*N}^i + \omega_{*T}^i$, where ω_{*N}^i and ω_{*T}^i are defined in the next subsection.

For the ITER case instead of using analytically prescribed functions for the pressure, density, temperature, and rotation, we will use profiles determined for the 9 MA ITER steady-state scenario target. Additionally, the ITER case will have three separate species, each with their own pressure: ions, electrons, and alpha particles. The following are given, as profiles of Ψ : $n_\alpha/(n_e + n_i)$, n_e , T_e , T_i , $P_\alpha/(P_e + P_i)$, and ω_ϕ . The ion density is taken to be equal to the electron density, ie. quasineutrality is not enforced. The ion and electron pressures are determined from $P_e = n_e T_e$, and $P_i = n_i T_i$, which then determines P_α as well.

For the ITER case instead of using analytically prescribed functions for the pressure, density, temperature, and rotation, we will use profiles determined for the 9 MA ITER target. The deuterium ion density is taken to be equal to the electron density (energetic particles, alpha

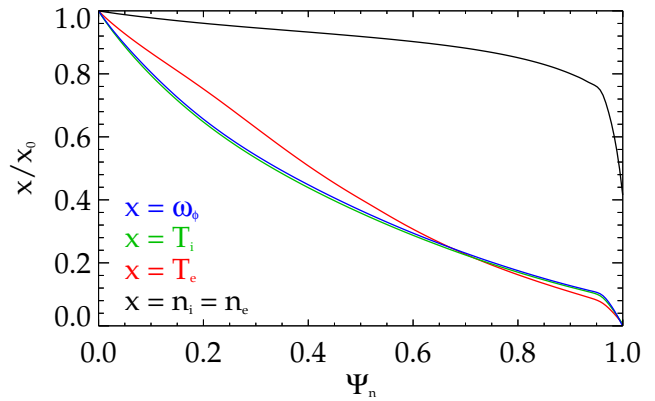


FIG. 5. Normalized profiles of density, temperature, and rotation for the ITER case.

particles, and tritium are not considered here). Figure 5 shows the profiles of density, temperature, and rotation, normalized to their axis values: $n_{i0} = n_{e0} = 7.22 \times 10^{19}$ m $^{-3}$, $T_{i0} = 31.32$ keV, $T_{e0} = 34.25$ keV, and $\omega_{\phi 0} = 37.34$ krad/s. The nominal value of ω_{E0}/ω_{A0} calculated from these parameters is 1.62×10^{-2} for the ITER case.

B. Diamagnetic Frequencies

The density and temperature gradient components of the diamagnetic frequency are defined in [rad/s] as: $\omega_{*N}^j = -T_j/(Z_j e n_j)(dn_j/d\Psi)$, $\omega_{*T}^j = -1/(Z_j e)(dT_j/d\Psi)$, where $Z_j e$ is the electric charge of species j . For the Solov'ev equilibria these can be written analytically as:

$$\omega_{*N}^i = -\omega_{*N}^e = \frac{0.7T_0/e}{(-\psi_0)} \left(\frac{1 - \Psi_n}{(1 - 0.7\Psi_n)^2} \right), \quad (9)$$

$$\omega_{*T}^i = -\omega_{*T}^e = \frac{0.3T_0/e}{(-\psi_0)} \left(\frac{1}{(1 - 0.7\Psi_n)^2} \right), \quad (10)$$

C. Collision Frequency

Although in general collisionality can impact kinetic stability calculations, and there are various ways of expressing collisionality²², for the comparisons here both ion and electron collision frequencies are taken to be zero. This decision was taken to avoid the complication of the effect of collisionality and to allow focus on the computation and comparison of other physics aspects in the codes.

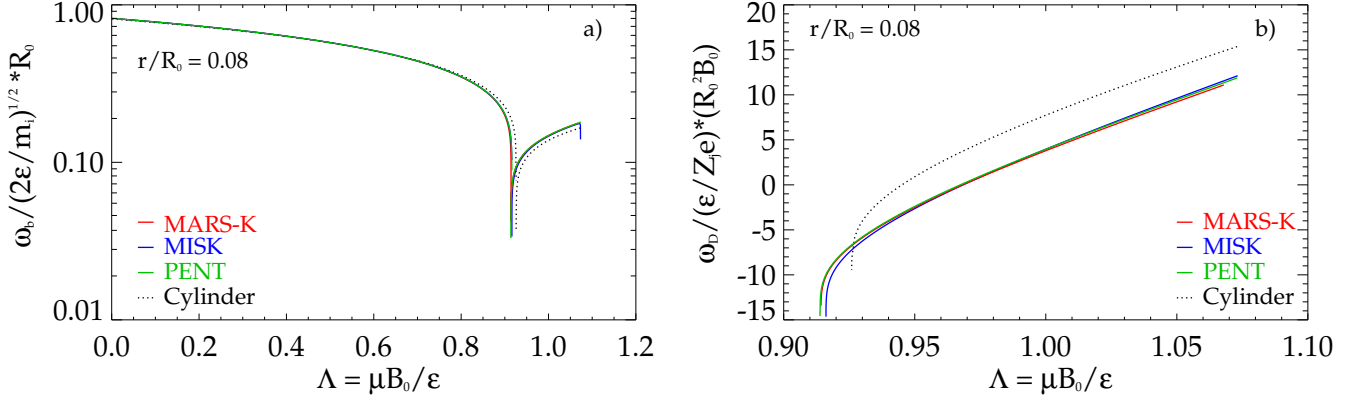


FIG. 6. a) Ion bounce frequency and b) ion magnetic precession drift frequency calculated by MISK, MARS-K, and PENT compared to the large aspect ratio approximation for the $\epsilon_r = 0.08$ surface of the Solov'ev 1 case, vs. Λ . The left branch of a) is for circulating ions and the right branch is for trapped ions. Plot b) can be directly compared to the same one produced by MARS-K in Ref. [14], Fig. 1(b).

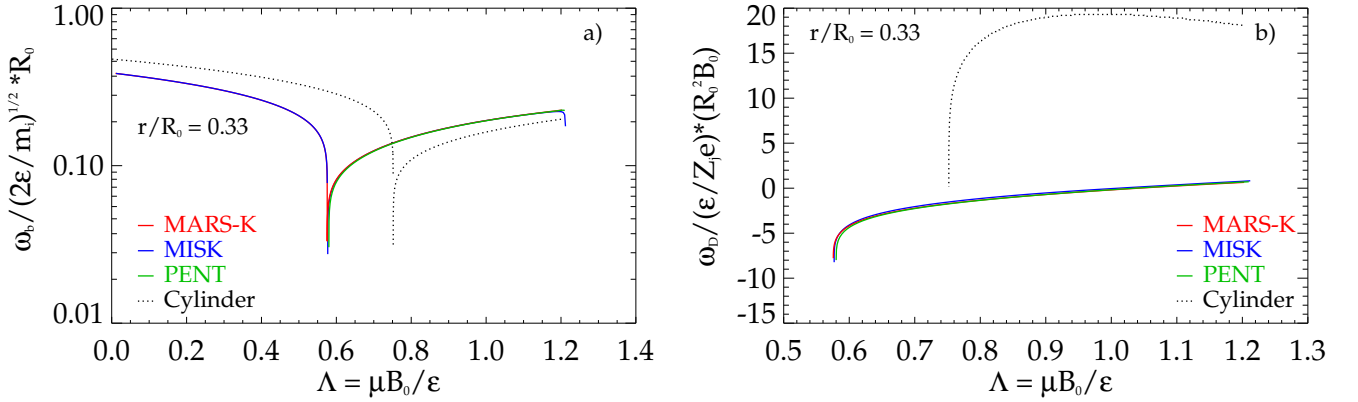


FIG. 7. a) Ion bounce frequency and b) ion magnetic precession drift frequency calculated by MISK, MARS-K, and PENT compared to the large aspect ratio approximation at the outer surface of the Solov'ev 3 case, vs. Λ . The left branch of a) is for circulating ions and the right branch is for trapped ions.

D. Bounce Frequency

The general formula for the particle bounce frequency is $\omega_b = 2\pi / (\int (d\ell / v_{\parallel}))$, where ℓ is the particle trajectory and v_{\parallel} is the parallel velocity.

In the large aspect ratio limit, the particle bounce frequency can be written^{13,67}:

$$\frac{\omega_b}{\sqrt{2\varepsilon/m_i}} = \frac{\sqrt{2\varepsilon_r\Lambda}}{4qR_0} \frac{\pi}{K(k)} \quad (\text{trapped}), \quad (11)$$

$$\frac{\omega_b}{\sqrt{2\varepsilon/m_i}} = \frac{\sqrt{1-\Lambda+\varepsilon_r\Lambda}}{2qR_0} \frac{\pi}{K(1/k)} \quad (\text{circulating}). \quad (12)$$

where Λ is a pitch angle variable defined by $\Lambda = \mu B_0 / \varepsilon$ with $\mu = mv_{\perp}^2 / 2B$ the magnetic moment and $\varepsilon = mv^2 / 2$ the kinetic energy of the particle (m and v are the mass

and velocity of the particle), K is the complete elliptic integral of the first kind, and

$$k = \left[\frac{1-\Lambda+\varepsilon_r\Lambda}{2\varepsilon_r\Lambda} \right]^{\frac{1}{2}}. \quad (13)$$

Figure 6a shows the normalized, dimensionless ion bounce frequencies calculated by MISK, MARS-K, and PENT compared to the large aspect ratio approximation, using the Solov'ev 1 equilibrium at the $\epsilon_r = 0.08$, $\Psi_n = 0.160$ surface vs. Λ . Figure 7a shows the normalized ion bounce frequencies compared to the large aspect ratio approximation, using the Solov'ev 3 equilibrium at the $\epsilon_r = 0.33$, $\Psi_n = 1$ surface (the plasma boundary) vs. Λ . Figure 8a shows the normalized ion bounce frequencies using the ITER equilibrium at the $\epsilon_r = 0.322$, $\psi_n = 0.982$ surface (very close to the plasma boundary) vs. Λ . All three codes are in quantitative agreement, and significantly deviate from the large aspect ratio case due to their general

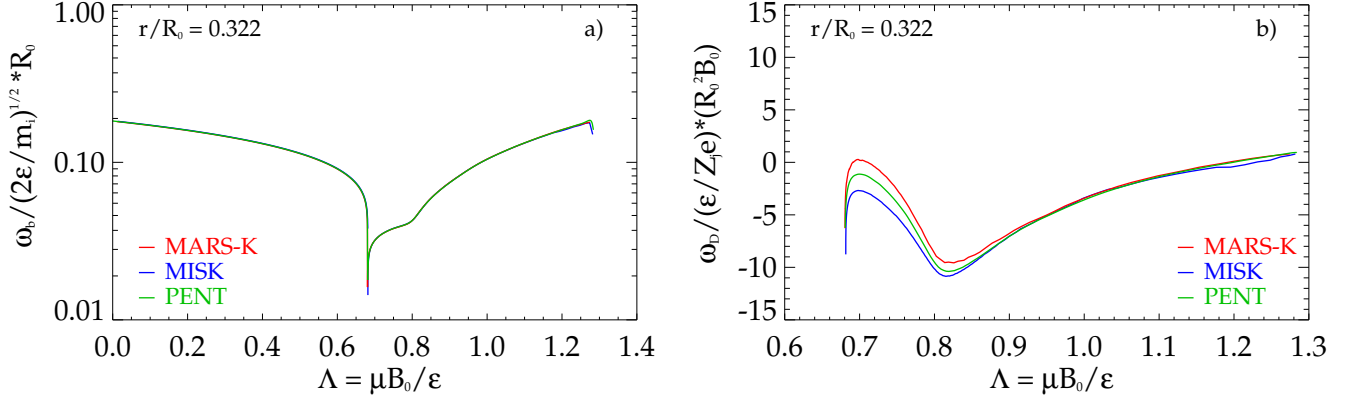


FIG. 8. a) Ion bounce frequency and b) ion magnetic precession drift frequency calculated by MISK, MARS-K, and PENT at the $\epsilon_r = 0.322$ surface (very close to the outer surface) of the ITER case, vs. Λ . The left branch of a) is for circulating ions and the right branch is for trapped ions.

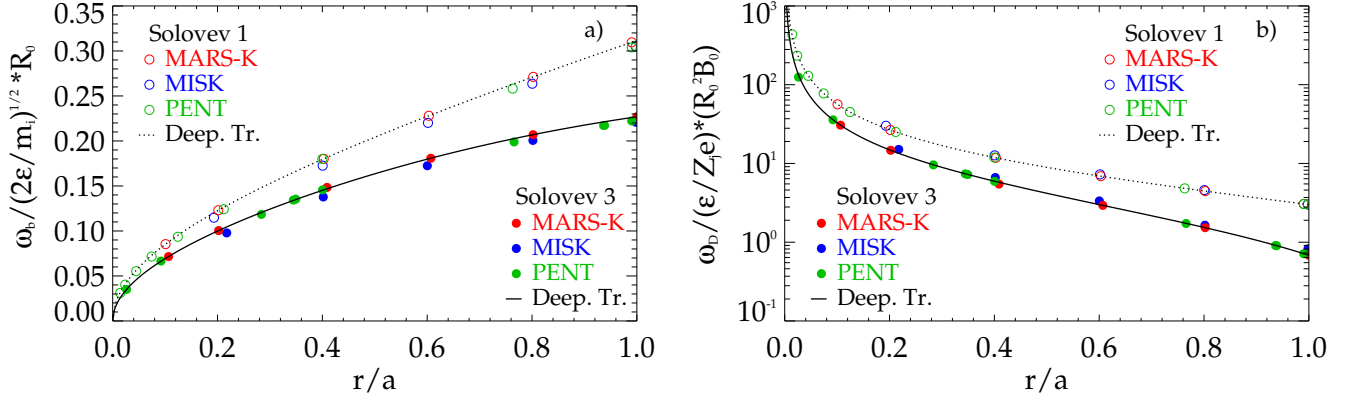


FIG. 9. a) Ion bounce frequency and b) ion magnetic precession drift frequency calculated by MISK, MARS-K, and PENT at maximum Λ compared to the deeply trapped particle limit for the Solov'ev 1 and 3 cases, vs. ϵ_r .

treatment of the magnetic topology.

In the limit of deeply trapped particles, one can show that for the Solov'ev equilibrium the bounce frequency can be written⁶⁵:

$$\frac{\omega_b}{\sqrt{2\epsilon/m_i}} = \frac{1}{q_0} \left(\frac{F^2}{1+2\epsilon_r} + \frac{\kappa^2 \epsilon_r^2}{q_0^2} \right)^{-1} \times \left[\frac{F^2 \epsilon_r}{2(1+2\epsilon_r)} + \frac{\kappa^2 \epsilon_r^3}{q_0^2} + \frac{(1-\kappa^2) \epsilon_r^2}{2q_0^2} (1+2\epsilon_r) \right]^{\frac{1}{2}} \quad (14)$$

Figure 9a shows the normalized ion bounce frequencies calculated by MISK, MARS-K, and PENT at maximum Λ compared to the deeply trapped particle limit, using the Solov'ev 1 and Solov'ev 3 equilibria vs. ϵ_r .

E. Magnetic Precession Drift Frequency

The general formula for the bounce-averaged magnetic precession drift frequency comes from Ref. [68], and is given by: $\omega_D = 1/(Z_j e)(\partial J/\partial \Psi)/(\partial J/\partial \epsilon)$, where $J = \int m_j v_{\parallel} d\ell$ is the equilibrium longitudinal invariant of the particle parallel motion. This equation for ω_D is broken into two parts. Using a definition of the bounce time, $\tau = \partial J/\partial \epsilon$,⁶⁸ we have:

$$\omega_D = \frac{\epsilon}{Z_j e \tau} \frac{1}{v^2} \frac{\partial}{\partial \Psi} \left(\int v_{\parallel} d\ell \right), \quad (15)$$

which eventually results in

$$\omega_D = -\frac{\epsilon}{Z_j e \tau} \int d\ell \left\{ \frac{1}{v_{\parallel}} \left[\frac{\Lambda}{B_0} \frac{\partial B}{\partial \Psi} \right] - \frac{2v_{\parallel}}{v^2} \left[\frac{B_{\theta}^2}{B} \frac{\partial}{\partial \Psi} \left(\frac{B}{B_{\theta}^2} \right) - \frac{1}{B_{\theta}^2} \left(\mu_0 \frac{\partial p}{\partial \Psi} + \frac{F}{R^2} \frac{\partial F}{\partial \Psi} \right) \right] \right\}, \quad (16)$$

Equation 16 is the form for ω_D used in MARS-K, with an equivalent expression used in MISK, while PENT uses an explicit bounce averaging of the gradient and curvature drift velocities⁴². Note that at the turning points $v_{\parallel} \rightarrow 0$ causes a singularity in Eq. 16, but this singularity is integrable.

The large aspect ratio magnetic precession drift frequency for trapped particles is^{13,14}:

$$\frac{\omega_D}{\varepsilon/(Z_j e)} = \frac{2q\Lambda}{R_0^2 \epsilon_r B_0} \left[(2s+1) \frac{E(k)}{K(k)} + 2s(k^2-1) - \frac{1}{2} \right], \quad (17)$$

where $s = (r/q)(dq/dr)$ is the magnetic shear and E is the complete elliptic integral of the second kind.

Figure 6b shows the normalized magnetic ion magnetic precession drift frequencies calculated by MISK, MARS-K, and PENT compared to the large aspect ratio approximation, using the Solov'ev 1 equilibrium at the $\epsilon_r = 0.08$, $\psi_n = 0.160$ surface, vs. Λ . Figure 7b shows the normalized ion precession drift frequencies compared to the large aspect ratio approximation, using the Solov'ev 3 equilibrium at the $\epsilon_r = 0.33$, $\psi_n = 1$ surface (the plasma boundary), vs. Λ . Figure 8b shows the normalized ion precession drift frequencies using the ITER equilibrium at the $\epsilon_r = 0.322$, $\psi_n = 0.982$ surface (very close to the plasma boundary) vs. Λ . Again, for ω_D all three codes are in quantitative agreement.

Finally, in the limit of deeply trapped particles, one can show that for the Solov'ev equilibrium the magnetic precession drift frequency can be written⁶⁵:

$$\frac{\omega_D}{\varepsilon/(Z_j e)} = \frac{q_0}{R_0 \kappa \epsilon_r} \left(\frac{F^2}{1+2\epsilon_r} + \frac{\kappa^2 \epsilon_r^2}{q_0^2} \right)^{-1} \left[\frac{F^2}{(1+2\epsilon_r)^2} - \frac{\kappa^2 \epsilon_r}{q_0^2} \right] \quad (18)$$

Figure 9b shows the normalized ion magnetic precession drift frequencies calculated by MISK, MARS-K, and PENT at maximum Λ compared to the deeply trapped particle limit, using the Solov'ev 1 and Solov'ev 3 equilibria vs. ϵ_r .

V. ENERGY INTEGRAL OF THE FREQUENCY RESONANCE FRACTION

A major part of the kinetic calculation (of $\tilde{\mathbb{P}}_K$ in Eq. 2) is the energy integration of the frequency resonance fraction:

$$I_{\varepsilon}(\Psi, \Lambda, l) = \int_0^{\infty} d\hat{\varepsilon} \left[\frac{n(\omega_{*N} + (\hat{\varepsilon} - \frac{3}{2})\omega_{*T}) + n\omega_E - \omega_r - i\gamma}{n\omega_D + (l + \alpha nq)\omega_b - i\nu_{\text{eff}} + n\omega_E - \omega_r - i\gamma} \hat{\varepsilon}^{\frac{5}{2}} e^{-\hat{\varepsilon}} \right]. \quad (19)$$

where $\hat{\varepsilon} = \varepsilon/T$, and $\alpha = 0$ for trapped particles or $\alpha = 1$ for circulating particles. Here l is the bounce harmonic and n is the toroidal mode number (not the density), and it will be taken as $n = -1$ for the comparisons presented here, to be consistent with the MARS-K geometrical convention. The energy integral can be evaluated based only upon the frequencies already described, for both ions and electrons. Nominally, $\nu_{\text{eff}} = 0$ as specified in subsection IV C, and we will take $\omega_r = 0$ and $\gamma = 0$. Note that when collisionality is zero, having a small imaginary component (via γ) in the denominator is beneficial to avoid singularities in the integration²⁴. Since we are taking $\nu_{\text{eff}} = 0$ and $\gamma = 0$, there are poles on the real energy axis, which need to be accounted for properly.

If we choose a particular Ψ surface, then ω_{*N} , ω_{*T} , and ω_E are constants. The precession drift and bounce frequencies are functions of both Λ and $\hat{\varepsilon}$ still, as indicated in Figs. 6 and 7.

One major historical difference between MISK and MARS-K is that MISK performed the energy integration numerically, whereas MARS-K performed it analytically¹³. Analytical solutions are possible only under certain constraints. For example, ν_{eff} must not have energy dependence and when $l \neq 0$ one must assume $\omega_D = 0$ ($\omega_D \ll \omega_b$). Since this is the approach taken in MARS-K and in MISK's analytical mode, we have used this assumption in PENT and in MISK's numerical mode for the purposes of this benchmarking. MARS-K, however, has recently implemented numerical integration, and can now treat energy-dependent collisionality. Therefore both MISK and MARS-K now have the capability to perform the energy integral either analytically or numerically. Although they were not used in that way in the present comparisons, in general each code can have energy-dependent collisionality and both precession and bounce frequencies simultaneously.

Performing the energy integration, we can plot I_{ε} as a function of Λ . Figure 10a shows each l component of $Re(I_{\varepsilon})$ from -2 to 2 for thermal ions in the Solov'ev 1 equilibrium at $r/R_0 = 0.08$ ($\Psi_n = 0.16$), the same surface chosen in Fig. 6. Figure 10b shows the same for the Solov'ev 3 equilibrium at $r/R_0 = 0.252$ ($\Psi_n = 0.585$, $q = 2.5$). Both of these are calculated at the nominal rotation of $\omega_{E0}/\omega_{A0} = 1 \times 10^{-2}$. The traces are plotted as l/n so that they are equivalent for $n = -1$ or $n = 1$. Note that while only the $l = -2$ to $l = 2$ bounce harmonics are shown and the contribution decreases with increasing $|l|$, many more bounce harmonics are included in the calculations in each code, to accurately capture the contribution from bounce resonant particles.

VI. EIGENFUNCTION COMPARISON

As an approximation to the fluid RWM, MISK and PENT use the marginally stable ideal kink eigenfunction with an ideal wall, as calculated by PEST and DCON, respectively (with differences described earlier), by moving

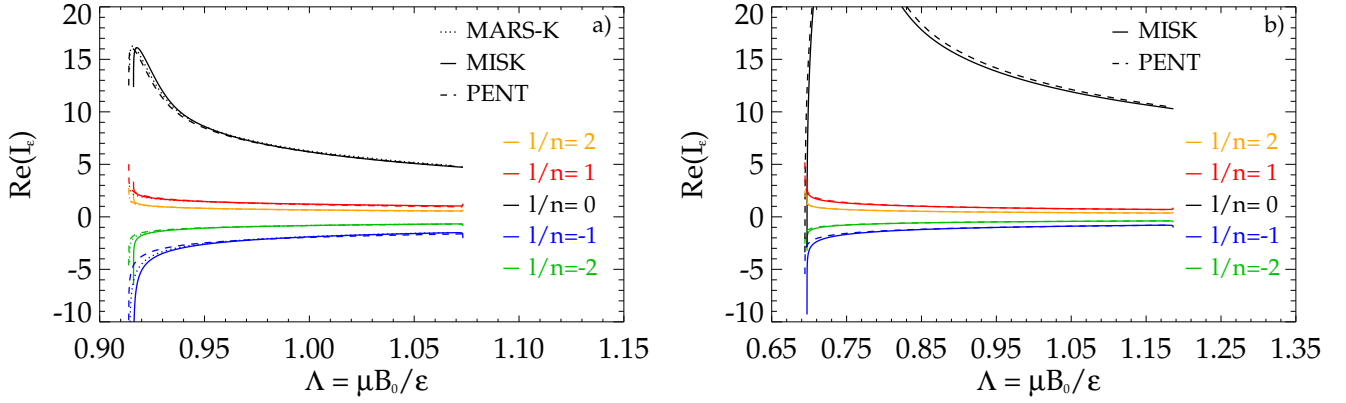


FIG. 10. Real components of I_ε for each l/n from -2 to 2, vs. Λ for thermal ions in the a) Solov'ev 1 equilibrium at $r/R_0 = 0.08$ ($\Psi_n = 0.16$), and b) the Solov'ev 3 equilibrium at $r/R_0 = 2.52$ ($\Psi_n = 0.585, q = 2.5$), calculated by MARS-K, MARS-K, and PENT in a) and MISK and PENT in b). In both cases, the nominal value of $\omega_{E0}/\omega_{A0} = 1 \times 10^{-2}$ was used.

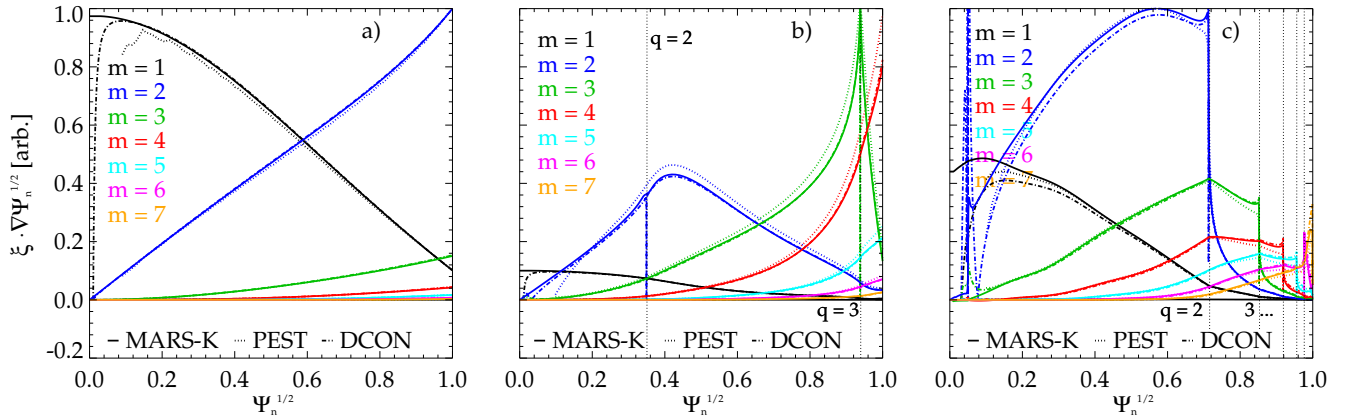


FIG. 11. Poloidal Fourier harmonics of the normal displacement for the marginally stable ideal kink mode with an ideal wall for a) the Solov'ev 1, b) the Solov'ev 3, and c) the ITER equilibria, as computed by PEST and DCON, compared to the fluid RWM eigenfunction as computed by MARS-K, in the PEST coordinate system.

the wall position progressively inward until the marginal point is found¹¹. This eigenfunction is a good approximation to the fluid RWM¹⁴, and has been compared to experiment³. Figure 11 compares the poloidal Fourier harmonics of the normal displacement $\xi \cdot \nabla \sqrt{\Psi_n}$ vs. $\sqrt{\Psi_n}$ for a marginally stable ideal kink mode with an ideal wall computed by PEST and DCON to the fluid RWM eigenfunctions computed by MARS-K for the two Solov'ev equilibria and the ITER equilibrium in PEST coordinates. The Fourier harmonics following this definition have more physical meaning (a better separation between resonant and non-resonant harmonics) than using equal-arc coordinates. Note that due to geometrical convention in the MARS-K code, both Solov'ev eigenfunctions will be considered to have $n = -1$ toroidal mode numbers.

VII. THE PERTURBED LAGRANGIAN

As will be shown in Eq. 21, another major part of the kinetic calculation is the perturbed Lagrangian¹⁴:

$$\langle H/\hat{\varepsilon} \rangle (\Psi, \Lambda, l) = \frac{1}{\tau} \oint \frac{1}{\sqrt{1 - \frac{\Lambda B}{B_0}}} e^{in\phi - i(l + \alpha n q)\omega_b t} \left[\left(2 - 3 \frac{\Lambda B}{B_0} \right) (\boldsymbol{\kappa} \cdot \boldsymbol{\xi}_\perp) - \left(\frac{\Lambda B}{B_0} \right) (\nabla \cdot \boldsymbol{\xi}_\perp) \right] d\ell. \quad (20)$$

Here $\langle \cdot \rangle$ indicates a bounce average, ϕ is the toroidal angle, and $\boldsymbol{\kappa} = \hat{\mathbf{b}} \cdot \nabla \hat{\mathbf{b}}$ is the magnetic curvature. Note that like the bounce and precession frequencies, this quantity has a singularity when $v_\parallel \rightarrow 0$, but it is integrable.

It is useful to examine the major constituents of $\langle H/\hat{\varepsilon} \rangle$ separately. Figure 12 shows an example $\nabla \cdot \boldsymbol{\xi}_\perp$ contour for the Solov'ev 3 equilibrium. Note

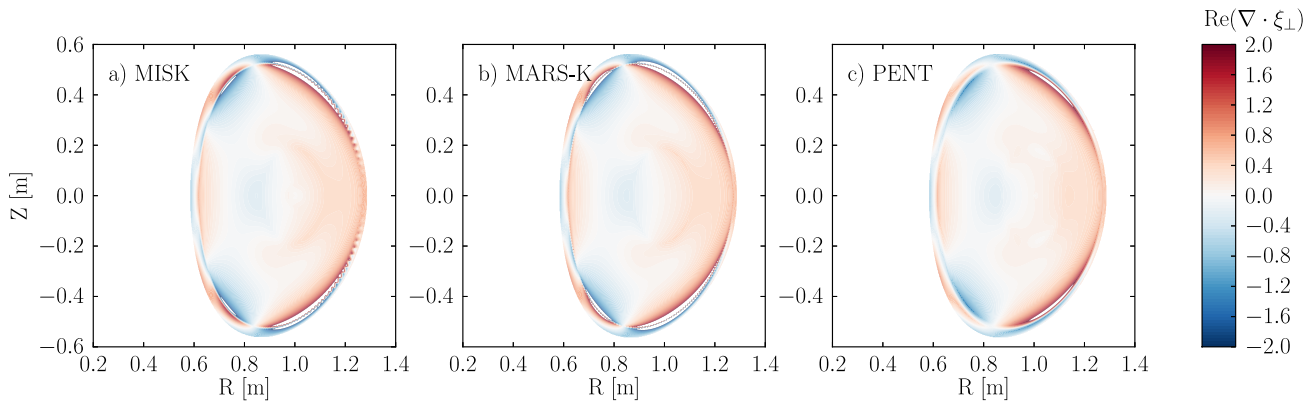


FIG. 12. $Re(\nabla \cdot \xi_{\perp})$ [arbitrary units] in the Solov'ev 3 equilibrium, calculated by a) MISK, b) MARS-K, and c) PENT. The MARS-K and PENT results are renormalized by making the maximum value at $r/R_0 = 0.252$ ($\Psi_n = 0.585, q = 2.5$) the same as the MISK maximum.

that $\kappa \cdot \xi_{\perp}$ and $\nabla \cdot \xi_{\perp}$ are related by the definition of the perturbed parallel magnetic field $\tilde{\mathbf{B}}_{\parallel} = -B(\nabla \cdot \xi_{\perp} + 2\kappa \cdot \xi_{\perp} - \xi_{\perp} \cdot \nabla(\mu_0 p/B^2))$.

Finally, one must be cautious in evaluating $\nabla \cdot \xi_{\perp}$, as the $\partial/\partial\phi$ component of $\nabla \cdot$ will change sign whether one uses $n = 1$ or -1 .

One concern is that at rational surfaces Alfvén resonances can lead to singularities in the calculation of δW_K ¹¹. We have found, however, that this is not the case at the $q = 2$ and $q = 3$ rational surfaces in the Solov'ev 3 calculation. Therefore in this case the integration is performed smoothly across these surfaces; no special considerations such as replacing the calculation in the vicinity of the rational surfaces with an analytic calculation^{20,69} are taken. Though no singularities were found in this case, small differences in the eigenfunction near the rational surfaces between the different codes *can* make a difference, as will be shown in Sec. IX B. In contrast, in the ITER case, singularities were found at the rational surfaces. The treatment of this issue will be discussed in Sec. IX B.

VIII. FLUID δW TERMS

δW_{∞} and δW_b are the fluid terms calculated with the wall at infinity or the actual “experimental” location b . In this study we will use a conformal wall, so that b is the distance of the wall away from the plasma boundary, in units of r/a , and the normalized wall position is $r_w/a = 1 + b$. The absolute value of these δW quantities as calculated by different codes is arbitrary (the normalizations and units differ); what really matters are the ratios. Therefore in this section we will report the quantity $\hat{\gamma}_f^{-1} = \delta W_b/(-\delta W_{\infty})$, which is the inverse fluid growth rate, normalized by the wall time.

Let us now also define $\delta W_{\infty} = \delta W_F + \delta W_S + \delta W_V^{\infty}$, the sum of the plasma fluid, surface, and vacuum perturbed potential energies when the wall is placed at infinity, and

$\delta W_b = \delta W_F + \delta W_S + \delta W_V^b$, the sum of the plasma fluid, surface, and vacuum δW terms when the wall is placed at a specific location b . The PEST and DCON codes use the VACUUM code⁷⁰ to calculate the δW_V terms. The plasma fluid terms are equal regardless of the wall position. The surface term arises when there is a finite pressure gradient at the plasma boundary. In the Solov'ev cases there is a gradient at the boundary, however the surface term is neglected for the purpose of this benchmarking exercise.

For the Solov'ev 1 case we choose conformal walls with $r_w/a = 1.15$, and for Solov'ev 3 $r_w/a = 1.10$ (see Fig. 1), to be consistent with Ref. [14]. For the ITER case, we choose a conformal wall with $r_w/a = 1.5$, which approximates the actual ITER wall position. See Fig. 3 for illustrations of these walls. The resulting values of $\hat{\gamma}_f^{-1}$ for Solov'ev 1 are 1.187, 1.122, and 1.120 for MARS-K, MISK, and PENT, respectively, for Solov'ev 3 are 1.830, 2.337, and 2.316 for MARS-K, MISK, and PENT, respectively, and for ITER are 0.682, 0.677, and 0.856 for MARS-K, MISK, and PENT, respectively.

Note that $\hat{\gamma}_f$ is slightly lower for MARS-K than PEST or DCON in the Solov'ev 1 case, and slightly higher in the Solov'ev 3 case. This will impact the kinetic growth rate, as will be seen in section X. For the ITER case DCON finds a lower $\hat{\gamma}_f$, due to a lower δW_{∞} . However, this difference also impacts the normalization of the kinetic effects in PENT so that in the end the ITER kinetic $\gamma\tau_w$ for PENT will be close to that of MARS-K and MISK.

IX. KINETIC δW_K

For trapped Maxwellian particles, the kinetic δW is given by

$$\delta W_K = -\frac{\sqrt{\pi}}{2} \int_0^{\Psi_a} \frac{nT}{B_0} \int_{B_0/B_{\max}}^{B_0/B_{\min}} \tau \sum_l |(H/\hat{\varepsilon})|^2 I_{\varepsilon} d\Lambda d\Psi, \quad (21)$$

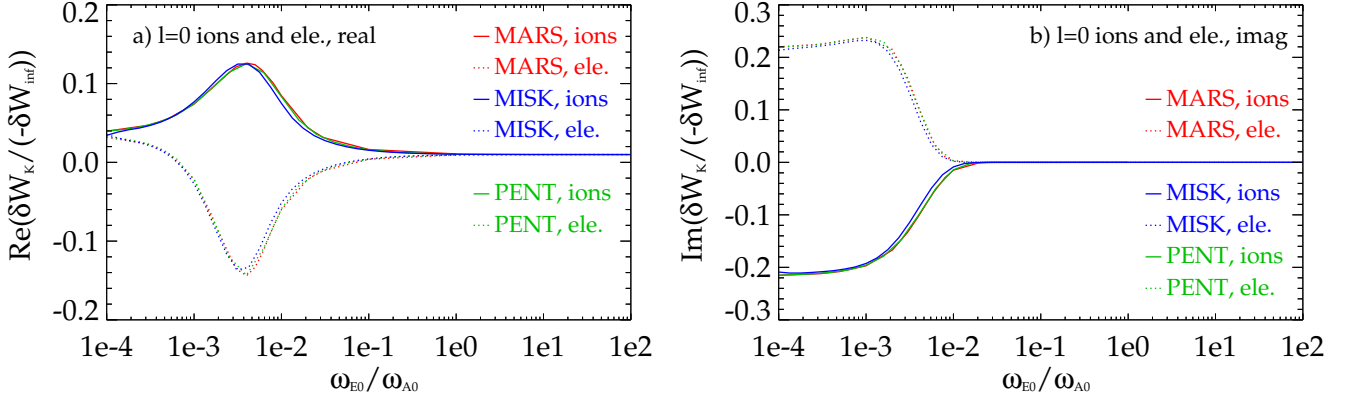


FIG. 13. a) Real and b) imaginary δW_K for $l = 0$ trapped thermal ions and electrons for the Solov'ev 1 case, as calculated by MARS-K, MISK, and PENT.

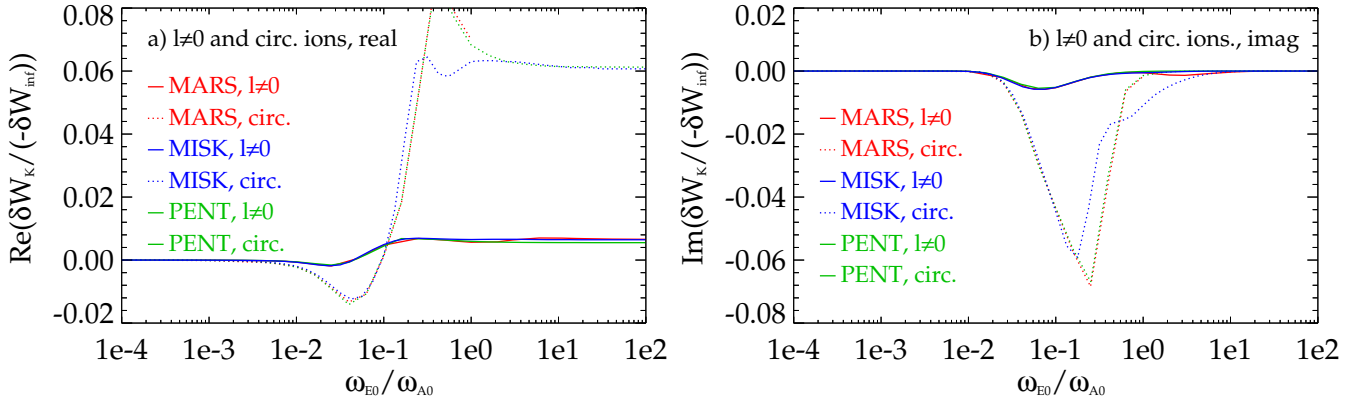


FIG. 14. a) Real and b) imaginary δW_K for $l \neq 0$ trapped thermal ions and for circulating ions for the Solov'ev 1 case, as calculated by MARS-K, MISK, and PENT.

where one can see that δW_K involves the previously defined quantities $I_{\hat{\varepsilon}}$ and $\langle H/\hat{\varepsilon} \rangle$ in a straightforward way.

Once again we will report the values found as $\delta W_K/(-\delta W_{\infty})$, broken into its various contributions in Figs. 13 and 14 for Solov'ev 1, Figs. 15 and 16 for Solov'ev 3, and Figs. 17 and 18 for ITER.

Generally, and as expected, one can see that the kinetic resonance between the mode and the precession motion of particles is strongest when the plasma rotation is small ($\omega_{E0}/\omega_{A0} \lesssim 0.1$), while the resonance with the bounce motion of trapped particles or circulating motion of passing particles is strongest at higher rotation ($\omega_{E0}/\omega_{A0} \gtrsim 0.1$). The codes agree well in the calculation of each term, especially for the precession resonance and especially for the Solov'ev 1 case, which has no rational surfaces. The rational surfaces are integrated over in the Solov'ev 3 case for each code. This is historically how PENT (with smoothed rational contribution) and MARS-K (unsmoothed) have been operated; MISK was operated like MARS-K in this case. This leads to the discrepancy between the codes in the bounce and circulating terms seen in Fig. 16, as we will discuss in Sec. IX B. Finally,

in the ITER case singular Alfvén resonances at the rationals have been removed for both MARS-K and MISK, and this leads to good agreement between each code in each term. This is how MISK has historically been operated (although the analytical replacement of the rational surface contribution normally calculated by MISK²⁰ was not included here); MARS-K was operated like MISK in this case. The PENT results are somewhat higher in magnitude in Figs. 17-18, due the lower δW_{∞} normalization factor. We have seen that this difference also affects the fluid growth rate, however, making γ_f^{-1} higher as well. Therefore the growth rate from PENT will be consistent with that of MISK and MARS-K in the end.

A. The CGL Limit

In the Chew-Goldberger-Low (CGL), or high-frequency limit, $|\omega_E - \omega| \rightarrow \infty$. Calculations in this limit of course represent an artificial scenario, as very high ω no longer applies to the RWM, and very high rotation loses touch with experimental reality and additionally

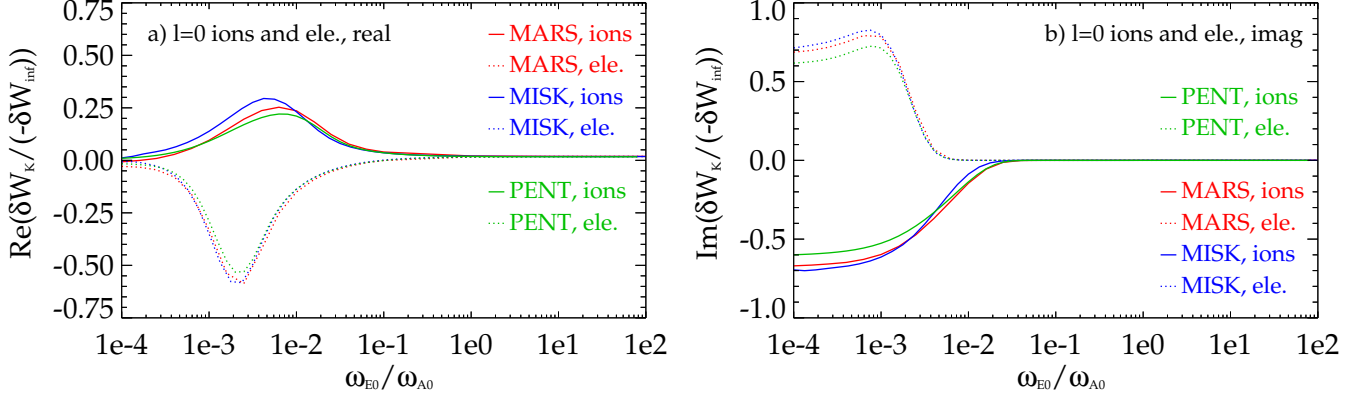


FIG. 15. a) Real and b) imaginary δW_K for $l = 0$ trapped thermal ions and electrons for the Solov'ev 3 case, as calculated by MARS-K, MISK, and PENT.

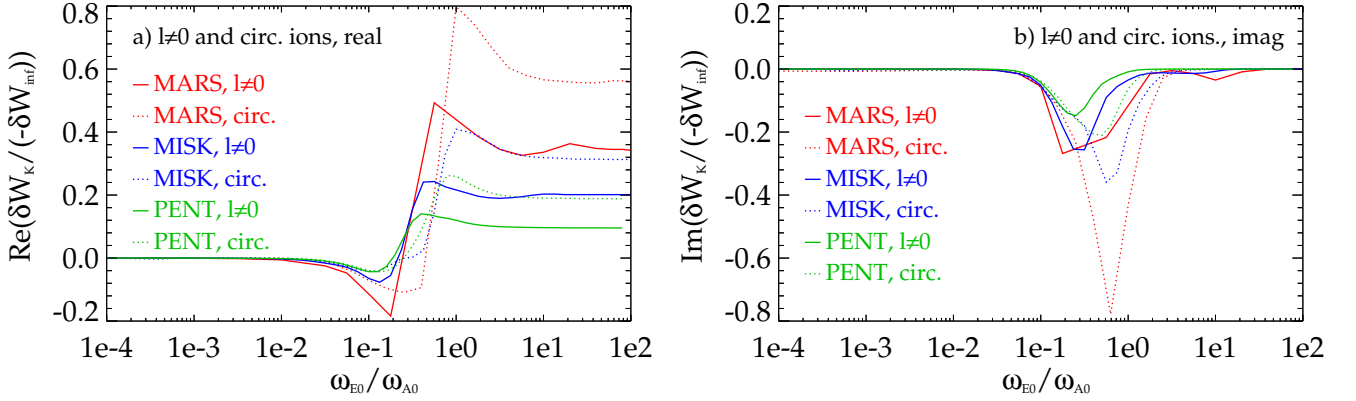


FIG. 16. a) Real and b) imaginary δW_K for $l \neq 0$ trapped thermal ions and for circulating ions for the Solov'ev 3 case, as calculated by MARS-K, MISK, and PENT.

we have neglected any effects of rotation on the equilibrium or fluid stability⁵¹. Nevertheless, in the CGL limit δW_K is purely real and independent of the mode-particle resonances, which allows a good check on the perturbed Lagrangian part of the problem. There are three separate possible ways to calculate δW in the CGL limit. The first is to just increase ω_E to a large value, as is effectively accomplished in Figs. 13-18 on the right hand side when $\omega_{E0}/\omega_{A0} = 100$. The total fluid δW_{CGL} is found by adding the various components in this limit. In this case circulating electrons and trapped electrons with a bounce ($l \neq 0$) resonance become important, so they are included as well. The second method is to add the various components while taking the analytical limit

$$I_\varepsilon(\Psi, \Lambda, l) \rightarrow I_\varepsilon^{CGL} = \int_0^\infty \hat{\varepsilon}^{\frac{5}{2}} e^{-\hat{\varepsilon}} d\hat{\varepsilon} = \frac{15\sqrt{\pi}}{8}. \quad (22)$$

These are effectively the numerical and analytical approaches, and give the same result. The third method is to solve for δW_{CGL} directly using the CGL perturbed pressures³⁶:

$$\delta W_{CGL} = \frac{1}{2} \int \frac{5}{3} p |\nabla \cdot \boldsymbol{\xi}_\perp|^2 dV + \frac{1}{2} \int \frac{1}{3} p |\nabla \cdot \boldsymbol{\xi}_\perp + 3\boldsymbol{\kappa} \cdot \boldsymbol{\xi}_\perp|^2 dV, \quad (23)$$

and then use the pressure and the quantities $\nabla \cdot \boldsymbol{\xi}_\perp$ and $\boldsymbol{\kappa} \cdot \boldsymbol{\xi}_\perp$ from section VII to calculate the fluid δW_{CGL} directly. The results of these methods are given in Table I for each case. Again, the differences between codes in the Solov'ev 3 case are due to integration over the rational surfaces, while the PENT ITER results are higher due to lower δW_∞ .

B. δW_K as a Function of Ψ

One can gain understanding of the importance of the core and edge regions, as well as rational surfaces, by

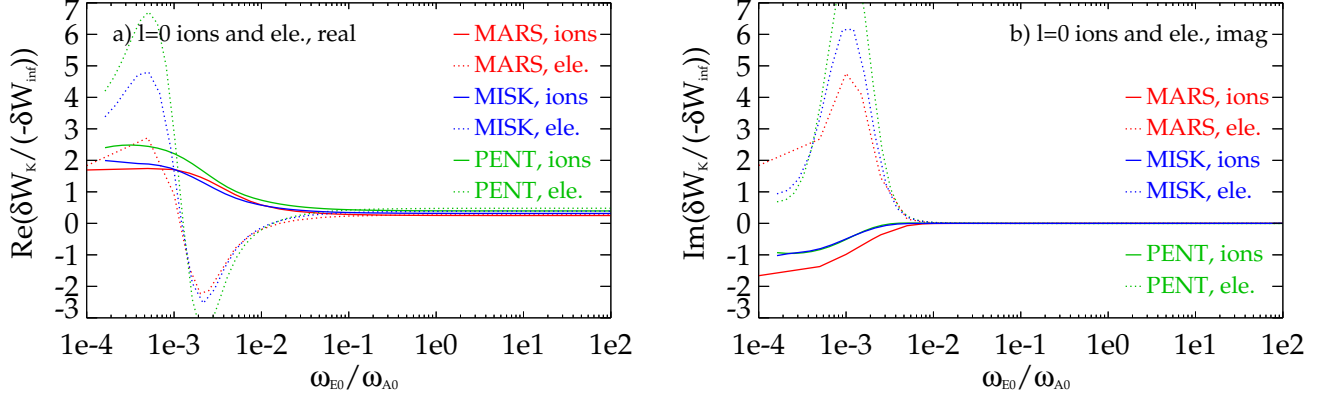


FIG. 17. a) Real and b) imaginary δW_K for $l = 0$ trapped thermal ions and electrons for the ITER case.

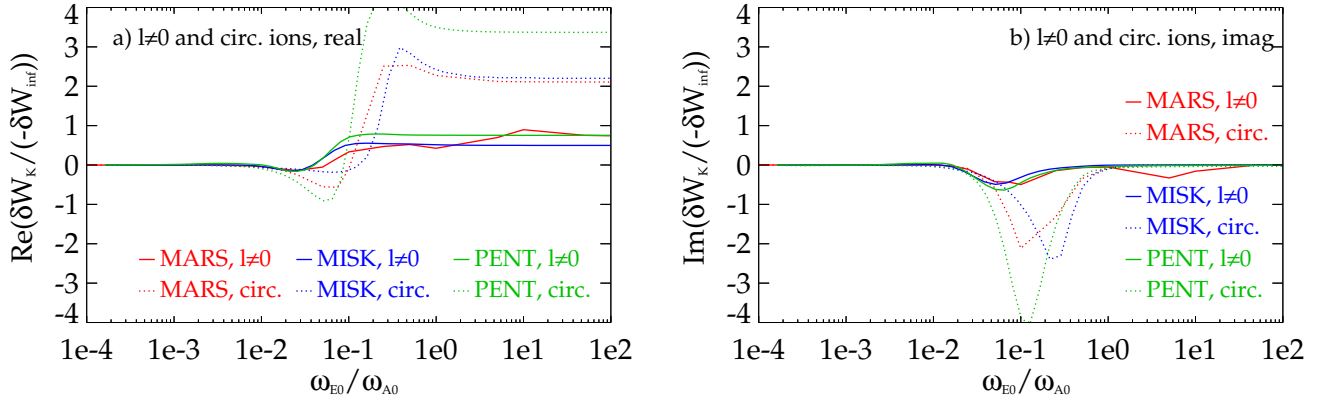


FIG. 18. a) Real and b) imaginary δW_K for $l \neq 0$ trapped thermal ions and for circulating ions for the ITER case.

	$\omega_{E0}/\omega_{A0} = 100$	Fluid δW_{CGL}
Solov'ev 1	1.57×10^{-1}	1.57×10^{-1}
	1.60×10^{-1}	1.56×10^{-1}
	1.55×10^{-1}	1.47×10^{-1}
Solov'ev 3	1.98×10^0	1.84×10^0
	1.10×10^0	1.01×10^0
	6.32×10^{-1}	6.36×10^{-1}
ITER	6.11×10^0	6.55×10^0
	6.72×10^0	6.53×10^0
	9.88×10^0	1.07×10^1

TABLE I. $\delta W_K/(-\delta W_\infty)$ in the CGL limit ($|\omega_E - \omega| \rightarrow \infty$). MARS-K results are on top, MISK results are in the middle, and PENT results are on the bottom. All values are real. For the ITER case surfaces within $\Delta q = \pm 0.1$ of all rational surfaces are excluded.

examining the contribution to δW_K as a function of Ψ . As an example, Fig. 19 shows $Re(d(\delta W_K/(-\delta W_\infty))/d\Psi)$ vs. Ψ for $l = 0$ and $l \neq 0$ trapped thermal ions in the Solov'ev 3 case at the CGL limit. The integrals of these curves represent the values of $Re(\delta W_K/(-\delta W_\infty))$ for $l =$

0 and $l \neq 0$ trapped thermal ions with $\omega_{E0}/\omega_{A0} = 1 \times 10^2$. The precession drift resonance calculation ($l = 0$) is much less sensitive to the rational surface, and the good agreement here in Fig. 19a explains the good agreement in Fig. 15a. The bounce resonance calculation ($l \neq 0$), however, is influenced by differences at the $q = 3$ rational surface. The differences in δW_K between the three codes in Fig. 16a at large rotation (on the right hand side) can be explained entirely by this difference at the rational surface.

Finally, however, in Fig. 20 for the ITER case (also in the CGL limit), it is clear that the rational surface contributions in the bounce resonance are not only very different between the codes, but unreasonably large for MISK and MARS-K. This is a well-known issue where singularities arise at the rational surfaces due to Alfvén resonances, and it was pointed out years ago¹¹. Generally, the treatment of this issue in MISK has been to remove the singular rational surface contributions calculated in this way by imposing a layer with width Δq around each rational surface, and then adding a separately calculated analytical Alfvén layer contribution²⁰. Note that this separate, analytical calculation was not added here, but

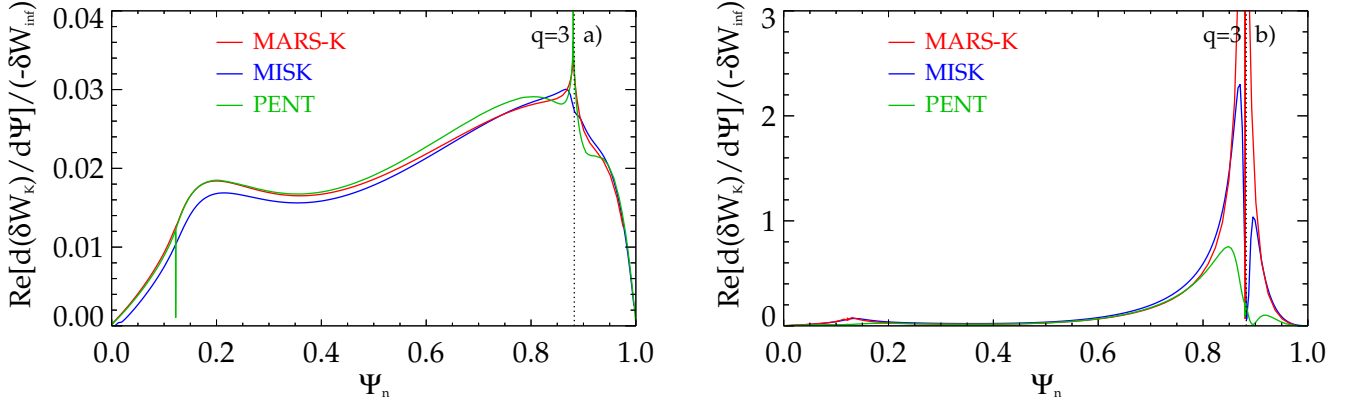


FIG. 19. $Re(d(\delta W_K)/(-\delta W_\infty))/d\Psi$ vs. Ψ for a) $l = 0$ trapped thermal ions and b) $l \neq 0$ trapped thermal ions in the Solov'ev 3 case at the CGL limit, as calculated by MARS-K, MISK, and PENT.

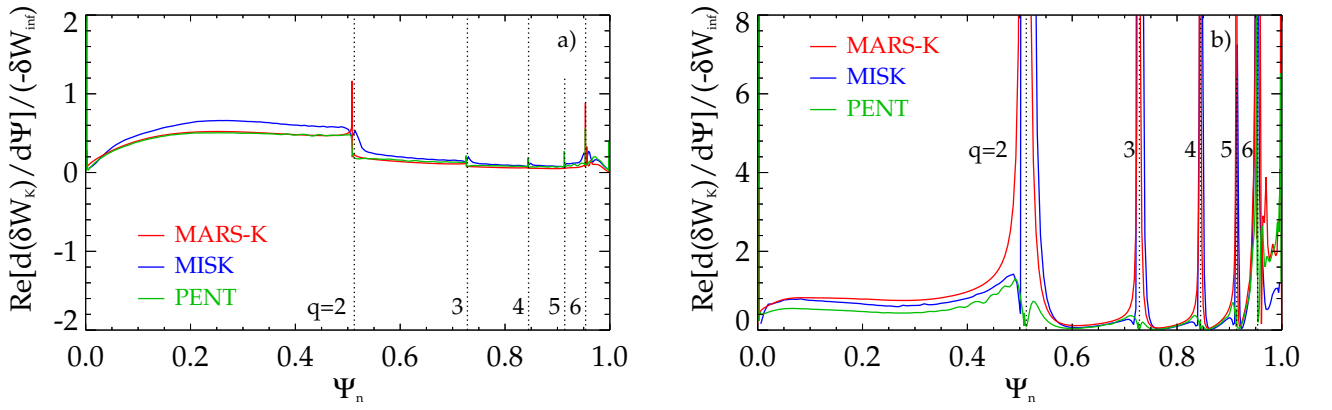


FIG. 20. $Re(d(\delta W_K)/(-\delta W_\infty))/d\Psi$ vs. Ψ for a) $l = 0$ trapped thermal ions and b) $l \neq 0$ trapped thermal ions in the ITER case at the CGL limit, as calculated by MARS-K, MISK, and PENT.

$\Delta q = 0.1$ was used for both MISK and MARS-K in this ITER case. Historically MARS-K has included the rational surface singularities in its calculations, which may account for some historical differences between the codes' results, particularly when MARS-K was operated in its perturbative mode. PENT, meanwhile, does not appear to have singularities in Fig. 20b. This is because the underlying IPEC calculation of the eigenfunction has been "regularized" at the rational surfaces with a standard and straightforward technique by using a characteristic width parameter σ such that $\xi \rightarrow \xi(m - nq)^2 / ((m - nq)^2 + \sigma)$, where m and n are the poloidal and toroidal mode numbers, respectively⁷¹. Essentially this approach smoothes the contribution to δW_K in a given width near the rational surfaces rather than simply removing it as in the MISK approach. One can see the effect of the IPEC approach for example in the Solov'ev 3 case (where the σ regularization was employed in IPEC but the Δq cut-off was *not* yet employed in MISK and MARS-K) in the lower values for PENT in Fig. 19.

X. GROWTH RATE AND MODE ROTATION FREQUENCY

In the dispersion relation (Eq. 1), the change in potential energy due to kinetic effects, δW_K , in general has both real and imaginary parts. The real part of ω is the mode rotation frequency and the imaginary part is the normalized growth rate. The results are given in Figs. 21, 22, and 23. They are in generally good agreement. Note that in Fig. 21a and in Fig. 22a at lower rotation the MARS-K $\gamma\tau_w$ differs from MISK and PENT due to difference in the fluid, not kinetic, δW_K terms, as can be seen by the dashed lines. For the Solov'ev 1 case, over a large range of rotation the growth rate is not substantially changed from the fluid case. The Solov'ev 3 case (Fig. 22) shows a larger influence of the kinetic effects. In particular, at high rotation the growth rate is reduced to different levels in each code's calculation due to the different levels of circulating and bounce resonant kinetic effects calculated. Intermediate plasma rotation is the least stable.

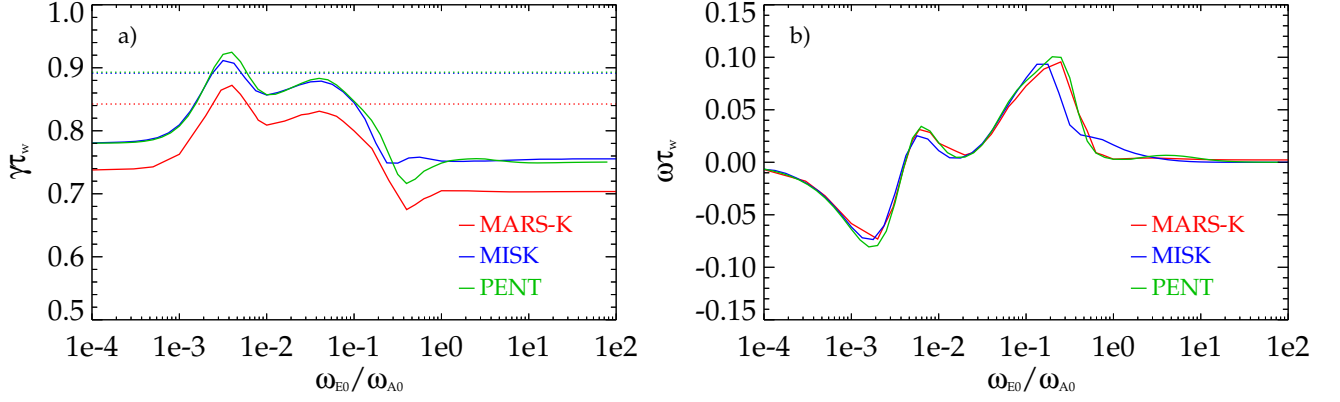


FIG. 21. a) $\gamma\tau_w$ (with $\gamma_f\tau_w$ shown in dashed lines) and b) $\omega\tau_w$ for the Solov'ev 1 case, as calculated by MARS-K and MISK.

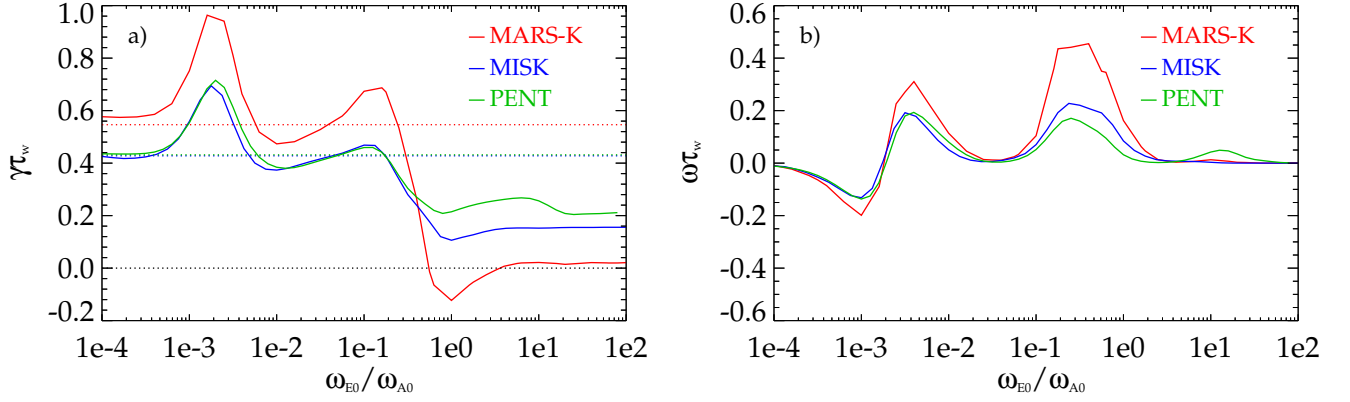


FIG. 22. a) $\gamma\tau_w$ (with $\gamma_f\tau_w$ shown in dashed lines) and b) $\omega\tau_w$ for the Solov'ev 3 case, as calculated by MARS-K and MISK.

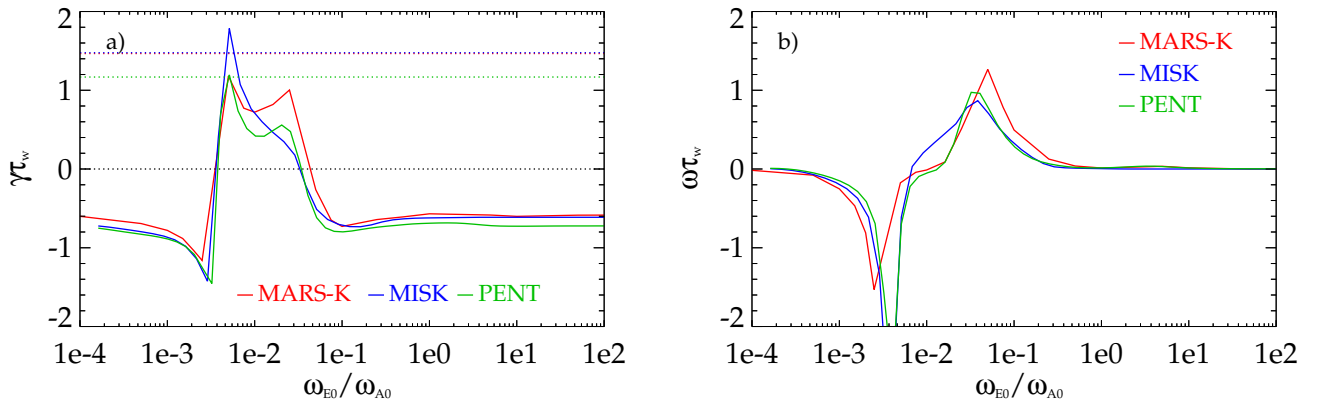


FIG. 23. a) $\gamma\tau_w$ (with $\gamma_f\tau_w$ shown in dashed lines) and b) $\omega\tau_w$ for the ITER case, as calculated by MARS-K and MISK.

	$\delta W_b/(-\delta W_\infty)(=\hat{\gamma}_f^{-1})$	$Re(\delta W_K)/(-\delta W_\infty)$	$Im(\delta W_K)/(-\delta W_\infty)$	$\gamma\tau_w$	$\omega_r\tau_w$
Solov'ev 1	1.187	2.18×10^{-2}	-1.21×10^{-2}	8.09×10^{-1}	1.82×10^{-2}
	1.122	2.08×10^{-2}	-6.82×10^{-3}	8.58×10^{-1}	1.11×10^{-2}
	1.120	2.14×10^{-2}	-1.14×10^{-2}	8.57×10^{-1}	1.86×10^{-2}
Solov'ev 3	1.830	7.94×10^{-2}	-1.47×10^{-1}	4.73×10^{-1}	1.14×10^{-1}
	2.337	8.92×10^{-2}	-8.96×10^{-2}	3.73×10^{-1}	5.07×10^{-2}
	2.316	7.13×10^{-2}	-1.39×10^{-1}	3.84×10^{-1}	8.02×10^{-2}
ITER	0.682	2.41×10^{-1}	-4.56×10^{-2}	8.19×10^{-1}	8.99×10^{-2}
	0.677	3.67×10^{-1}	-1.33×10^{-1}	4.64×10^{-1}	4.51×10^{-1}
	0.856	3.87×10^{-1}	-7.23×10^{-2}	4.89×10^{-1}	8.66×10^{-2}

TABLE II. A summary of important benchmarked quantities. MARS-K results are on top, MISK results are in the middle, and PENT results are on the bottom. For the Solov'ev 1 and 2 cases the nominal value of $\omega_{e0}/\omega_{A0} = 1 \times 10^{-2}$ is used. For the ITER case, the nominal value of $\omega_{e0}/\omega_{A0} = 1.62 \times 10^{-2}$ is used, and surfaces within $\Delta q = \pm 0.1$ of all rational surfaces are excluded.

The ITER case (Fig. 23) takes this trend even farther, as the kinetic resonances at high rotation with bounce and circulating particles is large enough in each code to stabilize the plasma, while the precession resonance at low rotation is as well. The intermediate rotation between these resonances remains vulnerable to instability (as is seen in experiments²⁰). One must recall that this is an incomplete calculation for ITER, however, as various simplifications have been made in the benchmarking process, including, most notably, the lack of collisions and energetic or alpha particles. Nevertheless, the codes agree in the basic underlying calculation of kinetic effects and all support the present understanding that both high and low rotation kinetic resonances are stabilizing to the RWM, but intermediate plasma rotation is potentially susceptible to instability.

Finally, table II shows a summary of important benchmarked quantities presented here. The calculated, and normalized, ideal δW_b , real and imaginary parts of the kinetic δW_K , growth rate, and mode rotation frequency are shown for each of the three cases with their respective chosen nominal rotation profiles, for each of the three codes. In some cases when the quantities are small, apparent discrepancies in this table can seem overstated when compared to the better-illustrated agreement in the corresponding ω_E scan plots already shown.

XI. COMPARISON OF MISK CALCULATIONS TO NSTX EXPERIMENTS

NSTX experiments have demonstrated unstable RWMs and MISK calculations have been used to understand those experimental results^{19–22,24,47,48}. Here we demonstrate that the benchmarked MISK calculations of thermal particle kinetic effects (now including collisions) can come close to predicting the marginal stability point. Figure 24 shows the calculated growth rate vs. scaled ex-

perimental rotation for two discharges from time points just before an unstable RWM caused a disruption (from Ref. [48]). In both cases MISK predicts that these discharges are close to marginal stability with the experimental rotation profile ($\omega_\phi/\omega_\phi^{\text{exp}} = 1$), and that both will go unstable with a slightly lower rotation, which is what actually happens in the experiment since the rotation is decreasing in time in these discharges and there is some further decrease from the equilibrium time points analyzed to the unstable time. We also can demonstrate, by the dashed lines in Fig. 24, that by integrating over the rational surfaces, rather than performing the calculation analytically, the code predicts significantly greater stability, which is inconsistent with the experimental ev-

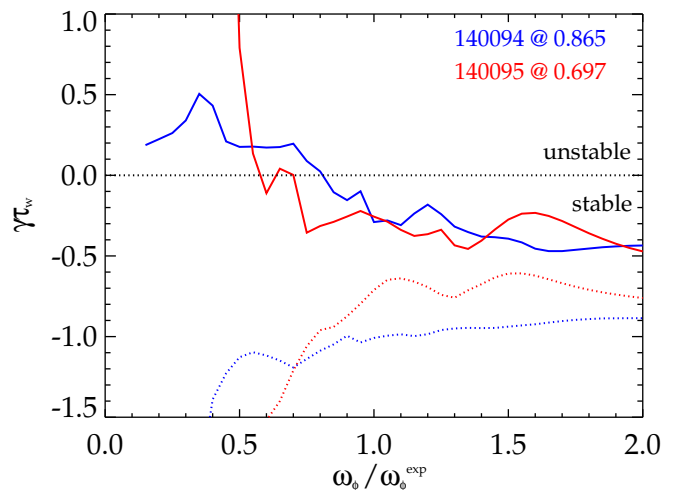


FIG. 24. $\gamma\tau_w$ vs. scaled experimental rotation profile as calculated by MISK for two NSTX equilibria near marginal RWM stability with the effect of the $n = 1$ rational surface singularities integrated numerically (dashed) or removed and replaced by an analytical calculation at the surfaces (solid).

idence, being well outside experimental error. Note that when the singularities are large enough and δW_K is larger than the fluid terms in Eq. 1, $\gamma\tau_w$ tends towards a highly stable value of unity.

XII. DISCUSSION AND CONCLUSIONS

Calculations of the kinetic effects on resistive wall mode stability with the MARS-K, MISK, and PENT codes have been benchmarked. During the course of this process, changes and improvements have been made to each of the codes. The successful development of the PENT code was concurrent with, and highly dependent upon this process. An error in the precession frequency calculation was successfully corrected in the MISK code. This change has been tested and found to have a moderate impact on previously published results because the precession frequency is much less than the rotation frequency in NSTX. Finally, an error in computing a particle phase factor in the bounce resonance of thermal ions in the MARS-K code was found and corrected.

The benchmarking exercise considered three cases: two analytical Solov'ev equilibria and a projected ITER equilibrium. The various important frequencies of the problem, including bounce and precession drift frequencies, have been compared and show good agreement between the codes and also with analytical limits. These frequencies are used in the energy integral of the frequency resonance fraction, which forms the heart of the problem of kinetic effects on RWM stability. Analytical solutions of the energy integral are possible under certain constraints, and comparisons show that there is good agreement between the numerical and analytical approaches, as well as between the codes. The marginally stable ideal kink (fluid RWM) eigenfunctions, which are not affected by kinetic effects in the perturbative calculations performed here, are compared and show good agreement for the three equilibria. The terms in the perturbed Lagrangian using the eigenfunction, $\kappa \cdot \xi_\perp$ and $\nabla \cdot \xi_\perp$, also generally agree between the codes, although differences exist at the rational surfaces. Ideal stability calculations of the fluid δW terms and fluid growth rates of the mode are consistent.

Finally, the kinetic δW terms, growth rates, and mode rotation frequencies have been compared between the codes for the two analytical Solov'ev equilibria and the projected ITER equilibrium. The codes all show good agreement in the most important kinetic terms: the $l = 0$ precession drift resonant (at $\omega_E \ll \omega_A$) trapped thermal ions and electrons. For bounce-resonant trapped particles and circulating ions, with resonance for $\omega_E \gtrsim 0.1\omega_A$, the codes show some disagreement at the rational surfaces of the Solov'ev 3 case when the surfaces are integrated over. This is also reflected in a disagreement of the real part of δW_K as $\omega_E \rightarrow \infty$ in the CGL limit. In the ITER case, once the singularities at the rational surfaces have been removed all three codes show good agreement

in δW_K .

The calculations shown here support the present understanding that RWM stability can be increased by kinetic effects at low rotation through precession drift resonance and at high rotation through bounce and transit resonances, while intermediate rotation can remain susceptible to instability. This can be most easily seen when the kinetic effects are used to calculate a growth rate and mode rotation frequency of the RWM. For example in Fig. 21a, for the Solov'ev 1 case, the growth rate is reduced at high and low ω_E . The results are in good agreement in this case, with the difference for $\gamma\tau_w$ coming mostly from the difference in the fluid growth rate (dashed lines). For the Solov'ev 3 case, the codes also show fairly good agreement in $\gamma\tau_w$ and $\omega\tau_w$, with the difference in $\gamma\tau_w$ at low ω_E again mostly due to the fluid growth rate, and the difference at high ω_E from the differences in the magnitude of the circulating and bounce resonances (Fig. 16), which comes from the rational surfaces. For MARS-K the rational surface contribution is large enough to provide marginal stability in this case. In the ITER case (Fig. 23) once the rational surface singularities are removed, the codes all agree well. The kinetic resonances at high rotation with bounce and circulating particles is large enough in each code to stabilize the plasma, while the precession resonance at low rotation is as well. The intermediate rotation between these resonances remains vulnerable to instability.

Comparisons between the benchmarked calculations of the MISK code and experimental marginal stability points from NSTX demonstrate that the kinetic stability code calculations are useful for predicting the stability of experimental devices. Additionally, it is conclusively shown that the numerically computed inclusion of the effect of rational surface singularities can lead to an unrealistically large predicted kinetic stabilization effect and incorrect prediction of very stable plasmas.

The successful benchmarking between MARS-K, MISK, and PENT gives great confidence that these codes are correctly calculating the theoretically important expected kinetic effects of resistive wall mode stability. To the extent that this model is then validated against present experimental evidence of RWM stability, one can then project the stability of future devices with confidence. This is important because reliable, validated resistive wall mode stability calculations are critical for ITER, which can not tolerate disruptions.

ACKNOWLEDGMENTS

The authors would like to thank Allen Boozer, Ian Chapman, Jonathan Graves, Jeremy Hanson, Kimin Kim, Jon Menard, and Holger Reimerdes for many fruitful discussions.

This paper is based upon a report made to the International Tokamak Physics Activity (ITPA). This research was supported by the U.S. Department of Energy un-

der contracts: DE-FG02-99ER54524 (Columbia University), DE-AC02-09CH11466 (Princeton Plasma Physics Laboratory), and DE-FG02-93ER54215 (University of Rochester). It was also supported in part by the Department of Energy Office of Science Graduate Fellowship Program (DOE SCGF), made possible in part by the American Recovery and Reinvestment Act of 2009, administered by ORISE-ORAU under Contract DE-AC05-06OR23100.

Additionally, this work was part-funded by the RCUK Energy Programme under grant EP/I501045 and the European Communities under the contract of Association between EURATOM and CCFE. To obtain further information on the data and models underlying this paper please contact PublicationsManager@ccfe.ac.uk. The views and opinions expressed herein do not necessarily reflect those of the European Commission.

- ¹M. S. Chu and M. Okabayashi, *Plasma Physics and Controlled Fusion* **52**, 123001 (2010).
- ²E. Strait, T. Taylor, A. Turnbull, J. Ferron, L. Lao, B. Rice, O. Sauter, S. Thompson, and D. Wroblewski, *Physical Review Letters* **74**, 2483 (1995).
- ³S. A. Sabbagh, A. C. Sontag, J. M. Bialek, D. A. Gates, A. H. Glasser, J. E. Menard, W. Zhu, M. G. Bell, R. E. Bell, A. Bondeson, C. E. Bush, J. D. Callen, M. S. Chu, C. C. Hegna, S. M. Kaye, L. L. Lao, B. P. LeBlanc, Y. Q. Liu, R. Maingi, D. Mueller, K. C. Shaing, D. Stutman, K. Tritz, and C. Zhang, *Nuclear Fusion* **46**, 635 (2006).
- ⁴A. Bondeson and D. Ward, *Physical Review Letters* **72**, 2709 (1994).
- ⁵R. Betti and J. P. Freidberg, *Physical Review Letters* **74**, 2949 (1995).
- ⁶R. Fitzpatrick and A. Y. Aydemir, *Nuclear Fusion* **36**, 11 (1996).
- ⁷A. C. Sontag, S. A. Sabbagh, W. Zhu, J. E. Menard, R. E. Bell, J. M. Bialek, M. G. Bell, D. A. Gates, A. H. Glasser, B. P. LeBlanc, K. C. Shaing, D. Stutman, and K. Tritz, *Nuclear Fusion* **47**, 1005 (2007).
- ⁸H. Reimerdes, A. M. Garafalo, G. L. Jackson, M. Okabayashi, E. J. Strait, M. S. Chu, Y. In, R. J. La Haye, M. Lanctot, Y. Liu, G. Navratil, W. Solomon, H. Takahashi, and R. Groebner, *Physical Review Letters* **98**, 055001 (2007).
- ⁹H. Reimerdes, A. M. Garafalo, M. Okabayashi, E. J. Strait, R. Betti, M. S. Chu, B. Hu, Y. In, G. L. Jackson, R. La Haye, M. Lanctot, Y. Liu, G. Navratil, W. Solomon, H. Takahashi, R. Groebner, and the DIII-D team, *Plasma Physics and Controlled Fusion* **49**, B349 (2007).
- ¹⁰B. Hu and R. Betti, *Physical Review Letters* **93**, 105002 (2004).
- ¹¹B. Hu, R. Betti, and J. Manickam, *Physics of Plasmas* **12**, 057301 (2005).
- ¹²B. Hu, R. Betti, and J. Manickam, *Physics of Plasmas* **13**, 112505 (2006).
- ¹³Y. Liu, M. S. Chu, C. G. Gimblett, and R. J. Hastie, *Physics of Plasmas* **15**, 092505 (2008).
- ¹⁴Y. Liu, M. S. Chu, I. T. Chapman, and T. C. Hender, *Physics of Plasmas* **15**, 112503 (2008).
- ¹⁵Y. Liu, M. S. Chu, I. T. Chapman, and T. C. Hender, *Nuclear Fusion* **49**, 035004 (2009).
- ¹⁶I. T. Chapman, V. G. Igochine, J. P. Graves, S. D. Pinches, A. Gude, I. Jenkins, M. Maraschek, and G. Tardini, *Nuclear Fusion* **49**, 035006 (2009).
- ¹⁷I. T. Chapman, C. G. Gimblett, M. P. Gryaznevich, T. C. Hender, D. F. Howell, Y. Q. Liu, and S. D. Pinches, *Plasma Physics and Controlled Fusion* **51**, 055015 (2009).
- ¹⁸Y. Liu, I. T. Chapman, M. S. Chu, H. Reimerdes, F. Villone, R. Albanese, G. Ambrosino, A. M. Garafalo, C. G. Gimblett, R. J. Hastie, T. C. Hender, G. L. Jackson, R. J. La Haye, M. Okabayashi, A. Pironti, A. Portone, G. Rubinacci, and E. J. Strait, *Physics of Plasmas* **16**, 056113 (2009).
- ¹⁹S. A. Sabbagh, J. W. Berkery, R. E. Bell, J. M. Bialek, S. P. Gerhardt, J. E. Menard, R. Betti, D. A. Gates, B. Hu, O. N. Katsuro-Hopkins, B. P. LeBlanc, F. M. Levinton, J. Manickam, K. Tritz, and H. Yuh, *Nuclear Fusion* **50**, 025020 (2010).
- ²⁰J. W. Berkery, S. A. Sabbagh, R. Betti, B. Hu, R. E. Bell, S. P. Gerhardt, J. Manickam, and K. Tritz, *Physical Review Letters* **104**, 035003 (2010).
- ²¹J. W. Berkery, S. A. Sabbagh, H. Reimerdes, R. Betti, B. Hu, R. E. Bell, S. P. Gerhardt, J. Manickam, and M. Podesta, *Physics of Plasmas* **17**, 082504 (2010).
- ²²J. W. Berkery, S. A. Sabbagh, R. Betti, R. E. Bell, S. P. Gerhardt, B. P. LeBlanc, and H. Yuh, *Physical Review Letters* **106**, 075004 (2011).
- ²³Y. S. Park, S. A. Sabbagh, J. W. Berkery, J. M. Bialek, Y. M. Jeon, S. H. Hahn, N. Eidietis, T. E. Evans, S. W. Yoon, J. Ahn, J. Kim, H. L. Yang, K. I. You, Y. S. Bae, J. Chung, M. Kwon, Y. K. Oh, W. Kim, J. Y. Kim, S. G. Lee, H. K. Park, H. Reimerdes, J. Leuer, and M. Walker, *Nuclear Fusion* **51**, 053001 (2011).
- ²⁴J. W. Berkery, R. Betti, and S. A. Sabbagh, *Physics of Plasmas* **18**, 072501 (2011).
- ²⁵H. Reimerdes, J. W. Berkery, M. J. Lanctot, A. M. Garafalo, J. M. Hanson, Y. In, M. Okabayashi, S. A. Sabbagh, and E. J. Strait, *Physical Review Letters* **106**, 215002 (2011).
- ²⁶G. Z. Hao, Y. Q. Liu, A. K. Wang, H. B. Jiang, G. Lu, H. D. He, and X. M. Qiu, *Physics of Plasmas* **18**, 032513 (2011).
- ²⁷D. Yadykin, Y. Q. Liu, and R. Paccagnella, *Plasma Physics and Controlled Nuclear Fusion* **53**, 085024 (2011).
- ²⁸I. T. Chapman, C. G. Gimblett, M. P. Gryaznevich, T. C. Hender, D. F. Howell, Y. Q. Liu, and S. D. Pinches, *Plasma Physics and Controlled Fusion* **53**, 065022 (2011).
- ²⁹I. T. Chapman, W. A. Cooper, J. P. Graves, M. P. Gryaznevich, R. J. Hastie, T. C. Hender, D. F. Howell, M. D. Hua, G. T. A. Huysmans, D. L. Keeling, Y. Q. Liu, H. F. Meyer, C. A. Michael, S. D. Pinches, S. Saarelma, and S. Sabbagh, *Nuclear Fusion* **51**, 073040 (2011).
- ³⁰G. Z. Hao, A. K. Wang, Y. Q. Liu, and X. M. Qiu, *Physical Review Letters* **107**, 015001 (2011).
- ³¹Z. R. Wang, S. C. Guo, and Y. Q. Liu, *Physics of Plasmas* **19**, 072518 (2012).
- ³²I. T. Chapman, Y. Q. Liu, O. Asunta, J. P. Graves, T. Johnson, and M. Jucker, *Physics of Plasmas* **19**, 052502 (2012).
- ³³I. B. Bernstein, E. A. Frieman, M. D. Kruskal, and R. M. Kulsrud, *Proceedings of the Royal Society of London. Series A, Mathematical and Physical Sciences* **244**, 17 (1958).
- ³⁴J. W. Van Dam, M. N. Rosenbluth, and Y. C. Lee, *Physics of Fluids* **25**, 1349 (1982).
- ³⁵T. Antonsen, "Theory of fusion plasmas," (Editrice Compositori, Bologna, 1987) Chap. Kinetic Energy Principles, pp. 161–183.
- ³⁶T. Antonsen, B. Lane, and J. Ramos, *Physics of Fluids* **24**, 1465 (1981).
- ³⁷T. Antonsen and Y. Lee, *Physics of Fluids* **25**, 132 (1982).
- ³⁸J. W. Van Dam, *Journal of the Korean Physical Society* **31**, S93 (1997).
- ³⁹S. Haney and J. Freidberg, *Physics of Fluids B* **1**, 1637 (1989).
- ⁴⁰R. Grimm, J. Greene, and J. Johnson, "Methods in Computational Physics, Vol. 16," (Academic Press, New York, 1976) Chap. Computation of the Magnetohydrodynamic Spectrum in Axisymmetric Toroidal Confinement Systems, pp. 253–280.
- ⁴¹Y. Liu, M. S. Chu, W. F. Guo, F. Villone, R. Albanese, G. Ambrosino, M. Baruzzo, T. Bolzonella, I. T. Chapman, A. M. Garafalo, C. G. Gimblett, R. J. Hastie, T. C. Hender, G. L. Jackson, R. J. La Haye, M. J. Lanctot, Y. In, G. Marchiori, M. Okabayashi, R. Paccagnella, M. Furno Palumbo, A. Pironti, H. Reimerdes, G. Rubinacci, A. Soppelsa, E. J. Strait, S. Ventre, and D. Yadykin, *Plasma Physics and Controlled Fusion* **52**, 104002 (2010).
- ⁴²N. C. Logan, J. K. Park, K. Kim, Z. Wang, and J. W. Berkery,

- Physics of Plasmas **20**, 122507 (2013).
- ⁴³I. T. Chapman, S. E. Sharapov, G. T. A. Huysmans, and A. B. Mikhailovskii, Physics of Plasmas **13**, 062511 (2006).
- ⁴⁴S. D. Pinches, L. C. Appel, J. Candy, S. E. Sharapov, H. L. Berk, D. Borba, B. N. Brieznan, T. C. Hender, K. I. Hopcraft, G. T. A. Huysmans, and W. Kerner, Computer Physics Communications **111**, 133 (1998).
- ⁴⁵M. Ono, S. M. Kaye, Y. K. Peng, G. Barnes, W. Blanchard, M. D. Carter, J. Chrzanowski, L. Dudek, R. Ewig, D. Gates, R. E. Hatcher, T. Jarboe, S. C. Jardin, D. Johnson, R. Kaita, M. Kalish, C. E. Kessel, H. W. Kugel, R. Maingi, R. Majeski, J. Manickam, B. McCormack, J. Menard, D. Mueller, B. A. Nelson, B. E. Nelson, C. Neumeyer, G. Oliaro, F. Paoletti, R. Parsells, E. Perry, N. Pomphrey, S. Ramakrishnan, R. Raman, G. Rewoldt, J. Robinson, A. L. Roquemore, P. Ryan, S. Sabbagh, D. Swain, E. J. Synakowski, M. Viola, M. Williams, and J. R. Wilson, Nuclear Fusion **40**, 557 (2000).
- ⁴⁶S. A. Sabbagh, J. W. Berkery, R. E. Bell, J. M. Bialek, S. P. Gerhardt, J. E. Menard, R. Betti, D. A. Gates, B. Hu, O. N. Katsuro-Hopkins, B. P. LeBlanc, F. M. Levinton, J. Manickam, K. Tritz, and H. Yuh, in *Proceedings of the 22nd IAEA Fusion Energy Conference, Geneva, Switzerland*, Vol. 1 (International Atomic Energy Agency, Vienna, 2008) pp. EX/5–1.
- ⁴⁷S. A. Sabbagh and The NSTX Team, Nuclear Fusion **53**, 104007 (2013).
- ⁴⁸J. W. Berkery, S. A. Sabbagh, A. Balbaky, R. E. Bell, R. Betti, A. Diallo, S. P. Gerhardt, B. P. LeBlanc, J. Manickam, J. E. Menard, and M. Podesta, [submitted to Physics of Plasmas](#) (2014).
- ⁴⁹Z. R. Wang, S. C. Guo, Y. Q. Liu, and M. S. Chu, Nuclear Fusion **52**, 063001 (2012).
- ⁵⁰S. C. Guo, X. Y. Xu, Z. R. Wang, and Y. Q. Liu, Nuclear Fusion **53**, 113035 (2013).
- ⁵¹J. Menard, Z. Wang, Y. Liu, S. M. Kaye, and J. K. Park, [submitted to Physical Review Letters](#) (2014).
- ⁵²K. C. Shaing, S. P. Hirshman, and J. D. Callen, Physics of Fluids **29**, 521 (1986).
- ⁵³C. Paz-Soldan, M. J. Lanctot, N. Logan, D. Shiraki, R. J. Buttery, J. M. Hanson, R. J. La Haye, J. Park, W. Solomon, and E. J. Strait, [submitted to Physics of Plasmas](#) (2014).
- ⁵⁴J. Park, Physics of Plasmas **18**, 110702 (2011).
- ⁵⁵Z. R. Wang, J. K. Park, Y. Q. Liu, N. Logan, K. Kim, and J. E. Menard, [submitted to Physics of Plasmas](#) (2013).
- ⁵⁶J. Park, A. H. Boozer, and A. H. Glasser, Physics of Plasmas **14**, 052110 (2007).
- ⁵⁷A. Glasser and M. Chance, Bulletin of the American Physical Society **42**, 1848 (1997).
- ⁵⁸J. Park, M. J. Schaffer, J. E. Menard, and A. H. Boozer, Physical Review Letters **99**, 195003 (2007).
- ⁵⁹J. Park, A. H. Boozer, J. E. Menard, S. P. Gerhardt, and S. A. Sabbagh, Physics of Plasmas **16**, 082512 (2009).
- ⁶⁰S. P. Gerhardt, J. E. Menard, J. K. Park, R. E. Bell, D. A. Gates, B. P. LeBlanc, S. A. Sabbagh, and H. Yuh, Plasma Physics and Controlled Nuclear Fusion **52**, 104003 (2010).
- ⁶¹A. M. Garofalo, W. M. Solomon, J. K. Park, K. H. Burrell, J. C. DeBoo, M. J. Lanctot, G. R. McKee, H. Reimerdes, L. Schmitz, M. J. Schaffer, and P. B. Snyder, Nuclear Fusion **51**, 083018 (2011).
- ⁶²J. Park, Y. M. Jeon, J. E. Menard, W. H. Ko, S. G. Lee, Y. S. Bae, M. Joung, K.-I. You, K.-D. Lee, N. Logan, K. Kim, J. S. Ko, S. Yoon, S. H. Hahn, J. H. Kim, W. C. Kim, Y.-K. Oh, and J.-G. Kwak, Physical Review Letters **111**, 095002 (2013).
- ⁶³L. Solov'ev, Zh. Eksp. Teor. Fiz. **53**, 626 (1967).
- ⁶⁴M. S. Chance, J. M. Greene, R. C. Grimm, J. L. Johnson, J. Manickam, W. Kerner, D. Berger, L. C. Bernard, R. Gruber, and F. Troyon, Journal of Computational Physics **28**, 1 (1978).
- ⁶⁵Y. Liu, R. J. Hastie, and T. C. Hender, Physics of Plasmas **19**, 092510 (2012).
- ⁶⁶F. Villone, Y. Liu, G. Rubinacci, and S. Ventre, Nuclear Fusion **50**, 125011 (2010).
- ⁶⁷A. Bondeson and M. S. Chu, Physics of Plasmas **3**, 3013 (1996).
- ⁶⁸M. Rosenbluth and M. L. Sloan, Physics of Fluids **14**, 1725 (1971).
- ⁶⁹L. J. Zheng, M. Kotschenreuther, and M. S. Chu, Physical Review Letters **95**, 255003 (2005).
- ⁷⁰M. Chance, Physics of Plasmas **4**, 2161 (1997).
- ⁷¹J. K. Park, *Ideal Perturbed Equilibria in Tokamaks*, Ph.D. thesis, Princeton University (2009).